



Université
de Toulouse

THÈSE

En vue de l'obtention du

DOCTORAT DE L'UNIVERSITÉ DE TOULOUSE

Délivré par :

Institut National Polytechnique de Toulouse (INP Toulouse)

Discipline ou spécialité :

Dynamique des fluides

Présentée et soutenue par :

M. DAMIEN SZUBERT

le lundi 29 juin 2015

Titre :

ANALYSE PHYSIQUE ET MODELISATION D'ECOULEMENTS
TURBULENTS INSTATIONNAIRES AUTOUR D'OBSTACLES
AERODYNAMIQUES A HAUT NOMBRE DE REYNOLDS PAR
SIMULATION NUMERIQUE

Ecole doctorale :

Mécanique, Energétique, Génie civil, Procédés (MEGeP)

Unité de recherche :

Institut de Mécanique des Fluides de Toulouse (I.M.F.T.)

Directeur(s) de Thèse :

MME MARIANNA BRAZA

M. GILLES HARRAN

Rapporteurs :

M. BRUNO KOOBUS, UNIVERSITE MONTPELLIER 2

M. GEORGE BARAKOS, UNIVERSITY OF LIVERPOOL

Membre(s) du jury :

M. ALAIN DERVIEUX, INRIA SOPHIA ANTIPOLIS, Président

M. FLAVIEN BILLARD, DASSAULT AVIATION, Membre

M. FRANK THIELE, TECHNISCHE UNIVERSITAT BERLIN, Membre

M. GILLES HARRAN, INP TOULOUSE, Membre

M. JEAN-PAUL DUSSAUGE, UNIVERSITE AIX-MARSEILLE 1, Membre

Mme MARIANNA BRAZA, INP TOULOUSE, Membre

Contents

Acknowledgements	iii
Nomenclature	v
1 Introduction	1
1.1 Objectives of this thesis	1
1.2 Governing equations in fluid dynamics	2
1.2.1 General transport equation	3
1.2.2 The Navier-Stokes equations	4
1.2.2.1 Continuity equation	4
1.2.2.2 Momentum equation	5
1.2.2.3 Energy equation	6
1.2.2.4 Additional relations	7
1.2.3 The Reynolds-averaged Navier-Stokes equations	8
1.2.4 The eddy-viscosity assumption	9
1.2.5 Organised-Eddy Simulation	9
1.3 Thesis outline	10
2 Tandem of two inline cylinders	13
2.1 Flow analysis - Static case	14
2.1.1 Context	14
2.1.2 Test-case description	15
2.1.3 Numerical method	16
2.1.4 Results	18
2.1.4.1 Flow overview	18
2.1.4.2 Convergence study	20
2.1.4.3 Turbulence model study	21
2.1.4.4 POD analysis	27
2.1.5 3D Simulations	41
2.2 Fluid-structure interaction - Dynamic case	43
2.2.1 Introduction	43
2.2.2 Results	43
2.2.2.1 Fluid-structure interaction	43
2.2.2.2 POD analysis	45
2.3 Conclusion	49

3 Physics and modelling around two supercritical airfoils	51
3.1 Shock-vortex shear-layer interaction in transonic buffet conditions	51
3.1.1 Shock-vortex shear-layer interaction in the transonic flow around a supercritical airfoil at high Reynolds number in buffet con- ditions	52
3.1.2 Upscale turbulence modelling	80
3.2 Laminar airfoil	81
4 Numerical study of an oblique-shock/boundary-layer interaction	117
5 Conclusion	129
Appendix A Turbulence models	135
A.1 One-equation eddy-viscosity models	135
A.1.1 Spalart-Allmaras model	135
A.1.2 Modified Spalart-Allmaras models	137
A.1.2.1 Edwards-Chandra model	137
A.1.2.2 Secundov's compressibility correction	137
A.2 Two-equation eddy-viscosity models	138
A.2.1 Chien's $k-\varepsilon$ model	138
A.2.2 Wilcox' $k-\omega$ model	139
A.2.3 Menter's $k-\omega$ models	139
A.2.3.1 Baseline model	139
A.2.3.2 Shear Stress Transport model	141
Appendix B $\gamma - R_\theta$ laminar/turbulent transition model	143
Appendix C Tecplot 360	147
C.1 Quick start	148
C.1.1 Load data	148
C.1.2 2D data	148
C.1.3 3D data	150
C.1.4 XY lines	151
C.1.5 Export and save	151
C.2 In more details	152
C.3 Scripting	154
C.3.1 Overview	154
C.3.2 Examples	154
Appendix D Monitoring files extractor GUI	157

Acknowledgements

These three years and half spent in the Institut de Mécanique des Fluides de Toulouse let me time and opportunities to meet many people, researchers, colleagues, students, and friends I want to thank here.

I want above all to express my deepest thanks to my supervisor Marianna BRAZA, who offered to me the opportunity to work in a practical way on fluid dynamics, and more particularly on turbulence modelling in the context of the Computational Fluid Dynamics, involving various test cases described in this manuscript. I was able to experience supervision of small groups of students, exchanging with them on technical and scientifical aspects. I also thank her a lot for helping me to survive in Stanford during summer 2014 after loosing my credit card, just before leaving France. Finally, I appreciated a lot the discussions we had concerning our vision of the World, society and humanity, with our respective experience and skills.

I am also very thankful to Prof. George Barakos for discussions we had regarding relations between research and industry, and for sharing is point of view regarding the situation of research more generally. I thank him as well as Flavien Billard, for their comments and corrections of this manuscript, as well as for sharing their special point of view on specific test cases.

I thank Prof. George Barakos and Prof. Bruno Koobus for having accepted the invitation to review my thesis. I also wish to thank all other members of the examining committee: Alain Dervieux, Jean-Paul Dussauge, Gilles Harran and Prof. Frank Thiele. I also thank Loïc Boudet, from DGA, and Prof. Julian Hunt, for taking part of the discussion during the defense. I would like to particularly thank Prof. Hunt for sharing his experience and his knowledge that conducted, among other, to the redaction of an article published in the Journal of Fluid Dynamics.

I want to express special thanks to Fernando Grossi, who helped a lot on physical and technical aspects when I arrived at IMFT for my internship and then for the beginning of my PhD while he was in first year of his PhD, as well as during congresses. I appreciated a lot his point of view regarding the environment and method of work.

I would not have been able to do all the work presented here without the precious assistance of Yannick Hoarau, regarding mesh generation in particular, but also for technical, programming aspects, despite his huge amount of work, and I am very grateful for this. For this last point, I also want to thank Jan Vos, from

[CFS Engineering](#), coordinator of the NSMB consortium, and who received me few days in his head quarters for implementing the transition model based on transport equations in NSMB.

My deepest gratitude to Parviz Moin, director of the Center for Turbulence Research, and his team, who received Marianna and me in Stanford during summer 2014, and Ik Jang, for the collaboration there. It was a great opportunity to discover a different work environment as well as the culture and lifestyle in Stanford and in the Bay Area in general.

I thank again Gilles Harran, as well as Alain Sévrain, for their precious contribution to improve my expertise in signal processing as well as in fluid-structure interactions.

My grateful thanks to Thibaut Deloze, Ioannis Asproulias, Wouter Van Veen, Antonio Jimenez Garcia, Saul Ferriera Perez, Vilas Shinde, Rogier Giepmans and the BEI students for their precious contributions to the work presented in this manuscript. I also thank them, as well as Rémi Bourguet, Johannes Scheller, Mathieu Marrant, Julie Albagnac, Simon Gsell and Christophe Korbuly for the enjoyable moments we had at the lab.

I thank all the services of the laboratory, from administration (Florence Colombies, Nadine Mandement, Aurélie Labrador, Denis Bourrel, Sandrine Chupin) to computing, reprography, documentation, as well as the direction of the lab, François Charru and Éric Climent, and of the group EMT2, Carlo Cossu, that allow researchers and students to work in a great environment in the IMFT and contribute to the cohesion of the research teams.

Finally, my relatives. First of all, Lucas, who offered me opportunities to breath, to relieve, to open my mind, and to consider more and less seriously the future. I thank him for this and for his support during tough moments, during the finale rush in particular. I thank also Yann, with whom I shared more or less a similar journey, and for funny and cultural moments we had in Toulouse as well as for the discussions about the world in general. Thank you Amély, for being there for years, even if I moved quite far from you and your little family. I gratefully thank my parents, who really cared about my appetite and curiosity to explore and discover that crazy, incredible world, as well as my brother and sister.

A huge thank to [Ciel mon doctorat](#). Any PhD student will understand.

The work presented in this memoir has been made possible thanks to the fellowship of the DGA ([Direction Général de l'Armement](#)) and the funding allocated by the ANR ([Agence Nationale pour la Recherche](#)) in the context of the Baresafe project (ANR-11-MONU-0004)

Nomenclature

Latin symbols

a	Speed of sound
c	Chord length
C_D	Drag coefficient
C_L	Lift coefficient
C_p	Pressure coefficient, $C_p = (P - P_\infty)/(0.5\rho_\infty U_\infty^2)$
d_w	Wall distance
D	Cylinder diameter
f_{VK}	Vortex-shedding frequency of the von Kármán instability
H	Shape factor
k	Turbulent kinetic energy
l	Turbulence length scale
L	Distance between cylinders center
P	Static pressure
Re	Chord and diameter-based Reynolds number
Re_θ	Momentum-thickness Reynolds number, $\rho\theta U_\infty/\mu$
$\text{Re}_{\theta t}$	Transition onset momentum-thickness Reynolds number
Re_ν	Vorticity Reynolds number, $\rho y^2 \Omega / \mu$
St	Strouhal number ($\text{St} = f_{VK} D / U_\infty$)
t	Physical time
t^*	Non-dimensionalised time ($t^* = tU_\infty/c$ or $t^* = tU_\infty/D$)
Tu	Turbulence intensity, $100(2k/3)^{1/2}/U$
U	Local velocity
U_∞	Inlet reference velocity
x_t	Laminar-turbulent transition location

Greek symbols

δ_{99}	Boundary-layer thickness
δ^*	Displacement thickness
δ_{ij}	Kronecker delta
ε	Turbulence dissipation rate
γ	Intermittency factor
γ_f, γ_{air}	specific heat ratio of the fluid and air
λ_θ	Pressure gradient parameter
μ	Dynamic viscosity
ν	Kinematic viscosity, μ/ρ
ν_t	Eddy viscosity
ω	Specific turbulence dissipation rate
Ω	Absolute value of vorticity
ρ	Fluid density
θ	Momentum thickness

Abbreviations

ATAAC	Advanced Turbulence Simulation for Aerodynamic Application Challenges
BSL	Menter's Baseline model
CFD	Computational Fluid Dynamics
DDES	Delayed Detached-Eddy Simulation
DNS	Direct Numerical Simulation
MIV	Movement induced vibration
NSMB	Navier-Stokes Multiblock
OSBLI	Oblique-shock/boundary-layer interaction
PIV	Particle Image Velocimetry
POD	Proper Orthogonal Decomposition
PSD	Power Spectral Density
RANS	Reynolds-averaged Navier-Stokes
RMS	Root mean square, $RMS(x) = \sqrt{1/N (x_1^2 + x_2^2 + \dots + x_N^2)}$
SA	Spalart-Allmaras one-equation model
SST	Shear Stress Transport model
SWBLI	Shock-wave/boundary-layer interaction
TFAST	Transition Location Effect on Shock-Wave/Boundary-Layer Interaction
TNT	Turbulent/non-turbulent
TUD	Technische Universiteit Delft or Delft University of Technology
URANS	Unsteady Reynolds-averaged Navier-Stokes
VIV	Vortex induced vibration
WM-LES	Wall-modelled Large Eddy Simulation

Mathematics

∇	Gradient, $\nabla \mathbf{U}(\mathbf{x}) = \left(\frac{\partial U_x(\mathbf{x})}{\partial x}, \frac{\partial U_y(\mathbf{x})}{\partial y}, \frac{\partial U_z(\mathbf{x})}{\partial z} \right)$, with $\mathbf{x} = (x, y, z)$
$\nabla \cdot$	Divergence, $\nabla \cdot \mathbf{U}(\mathbf{x}) = \operatorname{div}(\mathbf{U}(\mathbf{x})) = \frac{\partial U_x(\mathbf{x})}{\partial x} + \frac{\partial U_y(\mathbf{x})}{\partial y} + \frac{\partial U_z(\mathbf{x})}{\partial z}$
\otimes	Tensor product

Chapter 1

Introduction

Contents

1.1	Objectives of this thesis	1
1.2	Governing equations in fluid dynamics	2
1.2.1	General transport equation	3
1.2.2	The Navier-Stokes equations	4
1.2.2.1	Continuity equation	4
1.2.2.2	Momentum equation	5
1.2.2.3	Energy equation	6
1.2.2.4	Additional relations	7
1.2.3	The Reynolds-averaged Navier-Stokes equations	8
1.2.4	The eddy-viscosity assumption	9
1.2.5	Organised-Eddy Simulation	9
1.3	Thesis outline	10

1.1 Objectives of this thesis

The present thesis investigates high-Reynolds number unsteady turbulent flows interacting with the solid wall from the low subsonic to the high-transonic and supersonic regimes, by means of numerical simulation. A specific attention is paid to the prediction of unsteady separation, including fluid-structure interaction aspects, as well as shock/boundary-layer and shock-vortex interaction. A considerable effort is devoted in the state of the fundamental research and applications domains in order to improve the simulation and turbulence modelling approaches (statistical (RANS, URANS), Large-Eddy Simulations (LES) and Hybrid (RANS-LES)) for the prediction of unsteady separation and reattachment, of natural instabilities and vortex structures responsible for movement induced vibration and acoustic noise around bodies, as well as prediction of shock-wave/boundary-layer interaction, a crucial issue for next generation of ‘laminar’ wing design with reduced drag and

CO₂ emissions. A considerable effort is devoted internationally in order to provide more efficient High-Fidelity (Hi-Fi) approaches and to carry out modal analysis by suitable and specific methods, in order to elaborate reliable Reduced Order Modelling (ROM), which will allow for faster design cycles. The need of improvement of Hi-Fi and ROM approaches has been emphasized in a number of important international conferences as the 4th and 5th hybrid RANS-LES methods symposia (2012¹, 2014²), the ERCOFTAC symposium “Unsteady separation in Fluid-Structure interaction” 2013³, the biannual “Center for Turbulence Research” summer programme 2014⁴ and the “Whither Turbulence and Big Data” symposium 2015, among other. Through these meetings clearly appears the continuous need of advancing in turbulence modelling efforts in crucial regimes governed by strong adverse pressure gradients, by movement/deformation of the solid structure and by compressibility effects in order to provide more improved predictions for the design.

This thesis aims at contributing in this context by studying turbulence modelling approaches and their ability to capture important phenomena and crucial instabilities arising in aerodynamics and hydrodynamics, as well as the unsteady loads evolution, crucial for the design and to develop a detailed physical analysis of the flow phenomena arising in the near-wall and near-wake regions. Furthermore, it aims at providing a detailed modal analysis of the complex flow structure in order to prepare efficient reconstruction of the fields able to be used further on in ROM. These investigations have been carried out by means of well focused test-cases from the European Research programmes of the FP7: ATAAC⁵ (Advanced Turbulence simulations for Aerodynamic Application Challenges), coordinated by DLR - Göttingen, and TFAST⁶ (Transition location effect on shock wave boundary layer interaction), coordinated by IMP - Gdansk (Polish Academy of Science), as well as from the national ANR⁷ (Agence Nationale pour la Recherche) research programme Baresafe (Simulation of Safety Barrier Reliability), coordinated by EDF (Électricité de France).

1.2 Governing equations in fluid dynamics

In his Ph.D. thesis manuscript, Grossi (2014) described in a very comprehensive way the principles of the transport and governing equations in fluid dynamics. This section re-uses his work.

Fluid motion is governed by three fundamental laws: conservation of mass, of momentum and of energy. These principles can be expressed through conservation laws, which describe the evolution of the conserved quantities in a given domain by means of transport equations. In the governing equations of fluid dynamics the flowfield is treated as a continuous medium. This means that the mean free path of the fluid molecules is assumed to be very small compared to the length scale charac-

¹ Fu et al. (2012), <http://www.hrlm-4th.org>

² Girimaji et al. (2014)

³ <http://www.smartwing.org/ercoftac>

⁴ <https://ctr.stanford.edu>

⁵ <http://cfd.mace.manchester.ac.uk/ATAAC/WebHome>

⁶ <http://tfast.eu/>

⁷ <http://www.agence-nationale-recherche.fr>

teristic of the problem (e.g. the diameter of a cylinder or the chord of an airfoil) so that the interaction between the fluid molecules is much more important than their individual motion. Therefore, the whole system can be investigated using continuum mechanics imagining a fluid particle a as very large number of fluid molecules within a small volume. All flow properties (as velocity, pressure, temperature, viscosity, etc.) are in fact mean properties which reflect the statistical motion of the fluid molecules at each point of the flowfield.

1.2.1 General transport equation

Assuming that ϕ is a scalar conserved quantity per unit volume and that V is an arbitrary control volume fixed in space, the conservation law of ϕ states that the amount of this quantity inside V can vary as a result of its net flux across the surface S enclosing V and due to volume and surface sources of ϕ only. This law can be formalized in integral form as:

$$\frac{\partial}{\partial t} \int_V \phi dV = - \int_S (\mathbf{F}_C \cdot \mathbf{n}) dS - \int_S (\mathbf{F}_D \cdot \mathbf{n}) dS + \int_V Q_V dV + \int_S (\mathbf{Q}_S \cdot \mathbf{n}) dS. \quad (1.1)$$

The term on the left-hand side of Eq. 1.1 is the time variation of the total amount of ϕ inside V . The flux of ϕ across the volume boundaries is usually split into two components of different physical nature. \mathbf{F}_C is the ‘convective flux’, which corresponds to the time rate of ϕ crossing the surface S per unit surface. Convective fluxes are directional, being proportional to and aligned with the local flow velocity $\mathbf{U} = [U_x, U_y, U_z]^T$ and are given by $\mathbf{F}_C = \phi \mathbf{U}$. The second contribution, \mathbf{F}_D , is called ‘diffusive flux’ and is proportional and opposite to the gradient of ϕ . It is generalized by the ‘law of Fick’:

$$\mathbf{F}_D = -\kappa \rho \nabla \left(\frac{\phi}{\rho} \right). \quad (1.2)$$

where κ is a diffusivity coefficient. The physical mechanism of diffusion is related to molecular agitation and can have a net effect even in a fluid at rest if the distribution of ϕ is inhomogeneous. The minus signs in front of the fluxes are due to the fact that the surface normal vector \mathbf{n} is considered positive when pointing outwards (i.e. the dot products are negative when ϕ enters the control volume). Q_V and \mathbf{Q}_S are the volume and surface sources, respectively. The resulting expression is a convection-diffusion equation in integral form, which allows the fluxes to be discontinuous (as in the case of shock-waves). Moreover, in the absence of volume forces, the variation of the conserved variable inside the control volume depends only on the net flux of ϕ across the boundaries. A local differential form of the conservation law can be easily derived from the integral form. Using the divergence theorem (Gauss’ theorem), the surface integrals in Eq. 1.1 can be replaced by volume integrals of the divergences of the fluxes and surface sources. Also, assuming that the control volume is fixed in space, the time derivative on the left-hand side of the equation can be placed inside the integral (Reynolds’ transport theorem). Finally, since the integral form is written for an arbitrary control volume, the volume integrals can be dropped, yielding:

$$\frac{\partial \phi}{\partial t} = -\nabla \cdot \mathbf{F}_C - \nabla \cdot \mathbf{F}_D + Q_V + \nabla \cdot \mathbf{Q}_S, \quad (1.3)$$

which is valid at any point in the flowfield and requires the fluxes to be continuously differentiable (which is not always the case). It shows that surface sources are mathematically equivalent to fluxes and may be regarded in the same way. Moreover, if an equation is in conservative form, all the space derivative terms can be grouped as a divergence operator. Substituting the expressions obtained for the fluxes and rearranging the terms, one obtains:

$$\frac{\partial \phi}{\partial t} = -\nabla \cdot (\phi \mathbf{U}) + \nabla \cdot \left[\kappa \rho \left(\frac{\phi}{\rho} \right) \right] + Q_V + \nabla \cdot \mathbf{Q}_S. \quad (1.4)$$

In general, convective fluxes are non linear and yield first-order spatial derivatives while diffusive fluxes generate second-order ones. In the case where the conserved quantity is a vector, each component of ϕ can be regarded as a scalar quantity and the above equations can be applied. Alternatively, the equations written for a scalar property can be slightly modified, replacing the fluxes and surface sources by tensors and the volume source by a vector. Hence, the integral conservation equation for a vector reads:

$$\frac{\partial}{\partial t} \int_V \phi dV = - \int_S (\overline{\mathbf{F}_C} \cdot \mathbf{n}) dS - \int_S (\overline{\mathbf{F}_D} \cdot \mathbf{n}) dS + \int_V \mathbf{Q}_V dV + \int_S (\overline{\mathbf{Q}_S} \cdot \mathbf{n}) dS. \quad (1.5)$$

where $\overline{\cdot}$ stands for tensor. In differential form, Eq. 1.5 becomes:

$$\frac{\partial \phi}{\partial t} = -\nabla \cdot \overline{\mathbf{F}_C} - \nabla \cdot \overline{\mathbf{F}_D} + \mathbf{Q}_V + \overline{\mathbf{Q}_S}. \quad (1.6)$$

Using tensorial notation (for the sake of simplicity), the convective and diffusive fluxes are given by:

$$(F_C)_{ij} = \phi_i U_j, \quad (F_D)_{ij} = -\kappa \rho \frac{\partial}{\partial x_j} \left(\frac{\phi_i}{\rho} \right). \quad (1.7)$$

1.2.2 The Navier-Stokes equations

In this section, the three fundamental conservation laws that describe fluid motion are derived, namely the continuity equation, the momentum equation and the energy equation. For viscous flows, the resulting set of equations is commonly known as the ‘Navier-Stokes equations’.

1.2.2.1 Continuity equation

The principle of conservation of mass in a fluid is expressed through the continuity equation, which states that mass cannot be created nor destroyed in the system. The transported quantity is the fluid density ρ , which is a scalar quantity and has units of mass per unity volume. The continuity equation does not present a diffusive flux term since there is no mass diffusion in a fluid at rest. By replacing ϕ by ρ in

Eq. 1.1 and suppressing all source terms, the integral formulation of the continuity equation is obtained:

$$\frac{\partial}{\partial t} \int_V \rho dV + \int_S \rho (\mathbf{U} \cdot \mathbf{n}) ds = 0. \quad (1.8)$$

The term in the left-hand side of Eq. 1.8 represents the time rate of change of mass inside a given control volume and the surface integral on the right side is the total mass flow across its boundaries. For the latter, negative values mean a net flux entering the control volume while positive ones correspond to an outflow. Applying Gauss' and Reynolds' theorems, the continuity equation written in differential form reads:

$$\frac{\partial \rho}{\partial t} + \nabla \cdot (\rho \mathbf{U}) = 0. \quad (1.9)$$

For incompressible flows, ρ is constant and Eq. 1.9 reduces to $\nabla \cdot \mathbf{U} = 0$.

1.2.2.2 Momentum equation

Newton's second law states that the variation of the momentum of a body is equal to the net force acting on it. By applying this fundamental principle to a fluid, one obtains the momentum equation, which expresses the conservation of momentum in the fluid system. Since the momentum of a infinitesimally small fluid element of volume dV is defined as $\rho \mathbf{U} dV$, the transported variable in the momentum equation is the momentum per unit volume $\rho \mathbf{U}$, which is a vector quantity. Alternatively, the conservation of momentum can be expressed by means of three separated transport equations for the individual components of momentum ρU_x , ρU_y and ρU_z . As the continuity equation, the momentum equation has no diffusive flux since, by definition, the velocity (and thus the momentum) is zero in a fluid at rest. Hence, Eq. 1.5 applied for the transport of momentum yields:

$$\frac{\partial}{\partial t} \int_V \rho \mathbf{U} dV + \int_S \rho \mathbf{U} (\mathbf{U} \cdot \mathbf{n}) dS = \int_V \mathbf{Q}_V dV + \int_S (\overline{\mathbf{Q}}_S \cdot \mathbf{n}) dS. \quad (1.10)$$

where the volume sources \mathbf{Q}_V represent all existing body forces per unit volume, which act over dV and are also called external or volume forces (e.g. Coriolis, gravitational, centrifugal and electromagnetic forces). The surface sources $\overline{\mathbf{Q}}_S$ represent the second kind of forces that act on a fluid element: the surface (or internal) forces. In this group, there are the static pressure and the viscous stresses, which have a net effect only on the boundary of the volume. The pressure P exerted by the surroundings acts in the direction normal to S , pointing inwards the fluid element. Therefore, the surface sources can be computed as $-P \bar{\mathbf{I}} + \bar{\boldsymbol{\sigma}}$, where $\bar{\mathbf{I}}$ is the unit tensor and $\bar{\boldsymbol{\sigma}}$ is the viscous stress tensor. In aerodynamics, the effect of the gravitational force on the fluid elements can be neglected and other volume sources are usually not present. Hence, the momentum equation becomes:

$$\frac{\partial}{\partial t} \int_V \rho \mathbf{U} dV + \int_S \rho \mathbf{U} (\mathbf{U} \cdot \mathbf{n}) dS = - \int_S P (\bar{\mathbf{I}} \cdot \mathbf{n}) dS + \int_S (\bar{\boldsymbol{\sigma}} \cdot \mathbf{n}) dS, \quad (1.11)$$

or in differential form:

$$\frac{\partial \rho \mathbf{U}}{\partial t} + \nabla \cdot (\rho \mathbf{U} \otimes \mathbf{U}) = -\nabla P + \nabla \cdot \bar{\boldsymbol{\sigma}}. \quad (1.12)$$

Since air behaves as a Newtonian fluid, the shear stresses are proportional to the velocity gradients. Using tensorial notation, the general form of the viscous stress tensor σ_{ij} reads:

$$\sigma_{ij} = \mu \left(\frac{\partial U_j}{\partial x_i} + \frac{\partial U_i}{\partial x_j} \right) + \lambda \frac{\partial U_k}{\partial x_k} \delta_{ij}, \quad (1.13)$$

where the first index in the subscript indicates the direction normal to the plane on which the stress is acting while the second one gives its direction. If $i = j$ the component is a ‘normal stress’ and otherwise, a ‘shear stress’. Shear stresses are generated by the friction resulting from the relative motion of a body immersed in a fluid or of different fluid layers. In Eq. 1.13, μ is the dynamic viscosity and λ is the second viscosity of the fluid. According to Stoke’s hypothesis for a Newtonian fluid in local thermodynamic equilibrium:

$$\lambda + \frac{2}{3}\mu = 0. \quad (1.14)$$

This relation is called ‘bulk viscosity’ and is a property of the fluid. It is responsible for the energy dissipation in a fluid of smooth temperature distribution submitted to expansion or compression at a finite rate. So far, there is no experimental evidence that Eq. 1.14 does not hold except for extremely high temperatures or pressures. Using relation 1.14, Eq. 1.13 becomes:

$$\sigma_{ij} = \mu \left(\frac{\partial U_j}{\partial x_i} + \frac{\partial U_i}{\partial x_j} \right) - \frac{2\mu}{3} \frac{\partial U_k}{\partial x_k} \delta_{ij}. \quad (1.15)$$

Although the viscous stresses were derived as being surface sources, they play the role of diffusive fluxes of momentum (thus requiring fluid motion), with the dynamic viscosity acting as the diffusion coefficient.

1.2.2.3 Energy equation

In fluid dynamics, the conservation law for energy is obtained from the application of the first law of thermodynamics to a control volume. It expresses the fact that the time variation of the total energy inside a control volume is obtained from the balance between the work of the external forces acting on the volume and the net heat flux into it. In the energy equation, the transported quantity is the total energy per unit volume ρE , where E is the total energy per unit mass. It is defined as the sum of the internal energy per unit mass e (a state variable) and the kinetic energy per unit mass $|\mathbf{U}|^2/2$. The transport equation features a diffusive flux term which depends only on the gradient of e since, by definition, $\mathbf{U} = 0$ at rest. It accounts for the effects of thermal conduction related to molecular agitation and is given by $\mathbf{F}_D = -\gamma_f \rho \kappa \nabla e$, where γ_f is the ratio of specific heat coefficients of the considered fluid, $\gamma_f = c_p/c_v$. For dry air at 20°C, $\gamma_{air} = 1.4$. Since the internal energy can be expressed in terms of the static temperature T by $e = c_v T$, heat diffusion is more usually described using Fourier’s law:

$$\mathbf{F}_D = -\gamma_f \rho \kappa \nabla e = -\kappa \nabla T, \quad (1.16)$$

where k is the thermal conductivity coefficient ($k = c_p \rho \kappa$) and the negative sign accounts for the fact that heat is transferred from high- towards low-temperature regions.

Surface sources contribute to the energy equation through the work done by the pressure and viscous stresses (both normal and shear parts) acting on the boundaries of the fluid element $\mathbf{Q}_S = -p\mathbf{U} + (\bar{\sigma} \cdot \mathbf{U})$. Therefore, neglecting the work done by body forces as well as that of internal energy sources (e.g. radiation, chemical reactions, etc.), the integral form of the energy equation reads:

$$\begin{aligned} \frac{\partial}{\partial t} \int_V \rho E dV + \int_S \rho E (\mathbf{U} \cdot \mathbf{n}) dS &= - \int_S P (\mathbf{U} \cdot \mathbf{n}) dS \\ &\quad + \int_S (\bar{\sigma} \cdot \mathbf{U}) \cdot \mathbf{n} dS + \int_S k (\nabla T \cdot \mathbf{n}) dS, \end{aligned} \quad (1.17)$$

which is also frequently written in terms of the total enthalpy:

$$H = h + \frac{|\mathbf{U}|^2}{2} = E + \frac{P}{\rho}, \quad (1.18)$$

where h is the enthalpy per unit mass. This yields:

$$\frac{\partial}{\partial t} \int_V \rho E dV + \int_S \rho H (\mathbf{U} \cdot \mathbf{n}) dS = \int_S (\bar{\sigma} \cdot \mathbf{U}) \cdot \mathbf{n} dS + \int_S k (\nabla T \cdot \mathbf{n}) dS, \quad (1.19)$$

In differential form, Eq. 1.17 can be rewritten as:

$$\frac{\partial \rho E}{\partial t} + \nabla \cdot \rho \mathbf{U} E = -\nabla \cdot P \mathbf{U} + \nabla \cdot (\bar{\sigma} \cdot \mathbf{U}) + \nabla \cdot (k \nabla T). \quad (1.20)$$

1.2.2.4 Additional relations

In order to close the system of the Navier-Stokes equations, additional relations between the flowfield variables are needed. In aerodynamics, the air is usually modeled as a perfect gas and, therefore, a thermodynamic relation between the state variables P , ρ and T can be obtained by means of the equation of state:

$$P = \rho R T, \quad (1.21)$$

where $R = c_p - c_v$ is the gas constant per unit mass (for a perfect gas, c_p , c_v and thus γ_f and R are constants). In compressible viscous flow, heating due to high velocity gradients is responsible for variations in the fluid viscosity. To account for such effect, a common practice in aerodynamics is to adopt Sutherland's law (Sutherland, 1893), which expresses the dynamic viscosity μ of an ideal gas as a function of temperature only as:

$$\frac{\mu}{\mu_{\text{ref}}} = \left(\frac{T}{T_{\text{ref}}} \right)^{3/2} \frac{T_{\text{ref}} + S}{T + S}. \quad (1.22)$$

μ_{ref} is a reference viscosity corresponding to the reference temperature T_{ref} , and the constant S is the Sutherland's parameter (or Sutherland's temperature). Values commonly used for air are $\mu_{\text{ref}} = 1.715 \times 10^{-5}$ Pa.s, $T_{\text{ref}} = 273.15$ K and $S = 110.4$ K. Sutherland's Law gives reasonably good results at transonic and supersonic speeds. For hypersonic flows, however, more elaborated formulas are usually employed. The thermal conductivity coefficient k varies with temperature in a similar way to μ . For this reason, the Reynolds' analogy is frequently used to compute k , reading:

$$k = c_p \frac{\mu}{\text{Pr}} \quad (1.23)$$

where Pr is the Prandtl number, which is usually taken as 0.72 for air.

1.2.3 The Reynolds-averaged Navier-Stokes equations

According to 'Morkovin's hypothesis', the effect of density fluctuations on turbulent eddies in wall-bounded flows is insignificant provided that they remain small compared to the mean density. Indeed, this hypothesis is verified up to Mach numbers of about five (Blazek, 2005) and, therefore, a common approach in turbulence modeling is to apply 'Reynolds averaging' to the flow variables (otherwise one should use Favre averaging).

In Reynolds averaging, the flow variables are decomposed into two parts: a mean part and a fluctuating part. The velocity, for instance, is represented as $U = \bar{U} + U'$, where \bar{U} is its mean value and U' its instantaneous fluctuation. For stationary turbulent flows, \bar{U} is normally computed using time-averaging, which is the most common Reynolds-averaging procedure and is appropriate for a large number of engineering problems. Time-averaging can also be used for problems involving very slow mean flow oscillations that are not turbulent in nature, as long as the characteristic time scale of such oscillations is much larger than that of turbulence. In this way, the mean velocity is computed as:

$$\bar{U} = \lim_{T \rightarrow \infty} \int_t^{t+T} U dt \quad (1.24)$$

Also, by definition, the average of U' is zero. Substituting the flow variables in the Navier-Stokes equations by Reynolds-averaged ones and taking the average, obtains in differential form:

$$\frac{\partial \bar{\rho}}{\partial t} + \frac{\partial}{\partial x_i} (\bar{\rho} \bar{U}_i) = 0, \quad (1.25)$$

$$\frac{\partial}{\partial t} (\bar{\rho} \bar{U}_i) + \frac{\partial}{\partial x_j} (\bar{\rho} \bar{U}_i \bar{U}_j) = - \frac{\partial \bar{P}}{\partial x_i} + \frac{\partial}{\partial x_j} (\bar{\sigma}_{ij} + \tau_{ij}), \quad (1.26)$$

$$\frac{\partial}{\partial t} (\bar{\rho} \bar{E}) + \frac{\partial}{\partial x_j} (\bar{\rho} \bar{U}_j \bar{E}) = - \frac{\partial}{\partial x_j} (\bar{P} \bar{U}_j) + \frac{\partial}{\partial x_j} [(\bar{\sigma}_{ij} + \tau_{ij})] + \frac{\partial}{\partial x_j} \left(k \frac{\partial \bar{T}}{\partial x_j} + q_{tj} \right). \quad (1.27)$$

The only difference between the Reynolds-averaged Navier-Stokes (RANS) equations shown above and the original set of Navier-Stokes equations is the existence of a turbulent stress tensor $\tau_{ij} = -\bar{\rho} \bar{U}'_i \bar{U}'_j$ (also called Reynolds stress tensor) and

of a turbulent transport of heat q_{tj} . Both quantities are computed by means of additional equations (the so-called ‘turbulence models’) whose equations are reported in appendix A page 135.

1.2.4 The eddy-viscosity assumption

In the previous subsection, the Reynolds-averaged Navier-Stokes equations were presented and the turbulent stress tensor τ_{ij} and the turbulent heat flux q_{ij} were introduced. In this thesis, all turbulence models make use of Boussinesq hypothesis ([Boussinesq, 1877](#)), which relates the turbulent stresses to the mean-flow velocity gradients by:

$$\tau_{ij} = 2\mu_t S_{ij} - \frac{2}{3}\rho k \delta_{ij}, \quad (1.28)$$

where μ_t is a scalar ‘eddy viscosity’ (also called turbulent viscosity) and S_{ij} is the mean strain-rate tensor.

The Boussinesq hypothesis assumes that the principal axes of the turbulent stress and mean strain-rate tensors are collinear and is unable to capture anisotropy effects of the normal turbulent stresses. In practice, however, Eq. 1.28 provides accurate results for many engineering applications, including aerodynamic flows.

Based on the concept of eddy viscosity, the turbulent heat flux is then calculated by means of the ‘Reynolds analogy’:

$$q_{tj} = -k_t \frac{\partial T}{\partial x_j} = -c_p \Pr_t \frac{\mu_t}{\Pr_t} \frac{\partial T}{\partial x_j}, \quad (1.29)$$

where k_t is the turbulent thermal conductivity coefficient and \Pr_t is the turbulent Prandtl number (which for air is 0.9).

1.2.5 Organised-Eddy Simulation

Details of the Organised-Eddy Simulation (OES) method used in the 3D configuration of a tandem cylinders (chapter 2 page 13) as well as in the 2D simulation of a supercritical airfoil (chapter 3 page 51) have been published in [Bourguet et al. \(2008\)](#). This method was described as follows: The statistical turbulence modelling offers robustness of the simulations in this region at high Reynolds numbers but it has proven a strong dissipative character that tends to damp crucial instabilities occurring in turbulent flows around bodies, as for example low frequency modes as von Kármán instability, buffet or flutter phenomenon. The OES (Organised-Eddy Simulation) approach offers an alternative that is robust and captures the above physical phenomena. This approach consists in splitting the energy spectrum in a first part that regroups the organised flow structures (resolved part) and a second part that includes the chaotic processes due to the random turbulence (to be modelled). In the time-domain, the spectrum splitting leads to phase-averaged Navier-Stokes equations ([Jin and Braza, 1994](#)). A schematic illustration of the OES approach is presented in Fig. 1.1. The turbulence spectrum to be modelled is extended from low to high wavenumber range and statistical turbulence modelling considerations can be adopted inducing robustness properties. However, the use of standard URANS modelling is not sufficient in this case. In non-equilibrium turbulence, the inequality

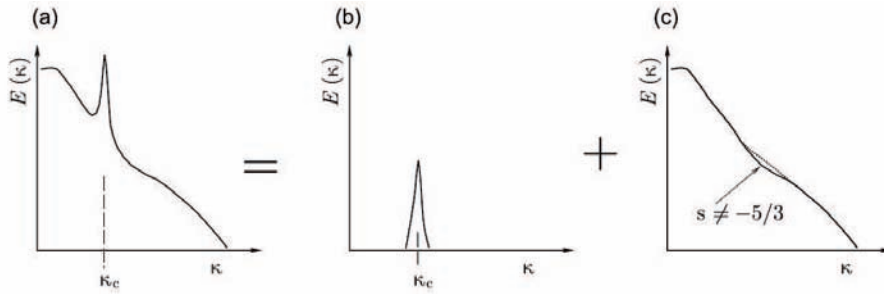


Figure 1.1: Sketch of the energy spectrum splitting in OES: (a) energy spectrum, (b) coherent part (resolved) and (c) random, chaotic part (modelled). k_c denotes coherent process wavenumber.

between turbulence production and dissipation rate modifies drastically the shape and slope of the turbulence spectrum in the inertial range (Fig. 1.1), comparing to the equilibrium turbulence, according to Kolmogorov's cascade (slope equals to $-5/3$). This modification has been quantified by the experimental study of [Braza et al. \(2006\)](#). Therefore, the turbulence scales used in standard URANS modelling have to be reconsidered in OES, to capture the effects due to the non-linear interaction between the coherent structures and the random turbulence. In the context of the OES approach, a modification of the turbulence scales in two-equation models was achieved on the basis of the second-order moment closure ([Bourdet et al., 2007](#)). By using the Boussinesq law 1.28 as well as the dissipation rate and the turbulent stresses evaluated by DRSM, a reconsidered eddy-diffusivity coefficient was derived. It was shown that the C_μ values were lower (order of 0.02) than the equilibrium turbulence value ($C_\mu = 0.09$) in two-equation modelling. Furthermore, the turbulence damping near the wall needed also to be revisited because of the different energy distribution between coherent and random processes in non-equilibrium near-wall regions. A damping law with a less abrupt gradient than in equilibrium turbulence was suggested, $f_\mu = 1 - \exp(-0.0002y^+ - 0.000064y^{+2})$ ([Jin and Braza, 1994](#)). The efficiency of the OES approach in 2D and 3D has been proven in a number of strongly detached high Reynolds number flows, especially around wings ([Hoarau et al., 2006](#)), as well as in the context of DES ([El Akoury, 2007](#)).

1.3 Thesis outline

This Ph.D. was a great opportunity to work on three main test-cases, covering a wide range of Mach numbers at high Reynolds numbers, by means of advanced statistical CFD methods.

The first configuration is a tandem of two inline cylinders at Mach number 0.12. The main flow features in static as well as in dynamic case, with the downstream cylinder free to move crosswise, is studied at this subsonic velocity. The results are given in chapter 2 (page 13). The transonic flow around two different supercritical airfoils, in the Mach number range 0.70–0.75, is next studied. Detailed results of the study around the OAT15A airfoil, involving time-frequency as well as POD analysis, and introducing a stochastic forcing method focussing on the Turbulent/-non-Turbulent interfaces prediction, are presented in chapter 3 (page 51) by means of

an article published in the Journal of Fluids and Structures ([Szubert et al., 2015b](#)) included in this manuscript. The V2C profil has also been studied in the context of the TFAST european project in 2D and 3D, involving laminar/turbulent transition location study, and the results have been detailed in an article submitted to the European Journal of Mechanics – B\Fluids, and also included in this manuscript (section [3.2](#) page [81](#). Finally, the predictive capabilities of a hybrid RANS-LES model, on the one hand, and of a wall-modelled LES, on the other hand, have been analysed during the summer programme 2014 handled by the Center for Turbulence Research, CA. All the results of this study are presented in chapter [4](#) (page [117](#)) by means of the proceeding following the programme. The last chapter (page [129](#)) is the conclusion of this manuscript. Appendices have also be written for extra contributions, such as a page/poster containing the equations of the $\gamma - \text{Re}_\theta$ two-equation transition model for implementation consideration, as this work as been done during this Ph.D., or a short user guide of the post-processing software Tecplot, for future users to benefit my knowledge of this complex but powerful software.

Chapter 2

Tandem of two inline cylinders

Contents

2.1 Flow analysis - Static case	14
2.1.1 Context	14
2.1.2 Test-case description	15
2.1.3 Numerical method	16
2.1.4 Results	18
2.1.4.1 Flow overview	18
2.1.4.2 Convergence study	20
2.1.4.3 Turbulence model study	21
2.1.4.4 POD analysis	27
2.1.5 3D Simulations	41
2.2 Fluid-structure interaction - Dynamic case	43
2.2.1 Introduction	43
2.2.2 Results	43
2.2.2.1 Fluid-structure interaction	43
2.2.2.2 POD analysis	45
2.3 Conclusion	49

The tandem cylinder arrangement is a canonical problem to advance modeling techniques for flow interactions. Tandem cylinders with similar diameters can be found in several locations on a landing gear, such as multiple wheels, axles, and hydraulic lines. This configuration can be found in cooling, venting systems, or platform support. In section 2.1, the modelling capabilities as well as the physics around two static inline cylinders are studied. In section 2.2, the fluid-structure problems are considered by giving one degree of freedom in translation to the downstream cylinder.

2.1 Flow analysis - Static case

2.1.1 Context

The 36-month ATAAC (Advanced Turbulence Simulation for Aerodynamic Application Challenges) European project, ended in 2012, handled several geometries with the aim of investigating the capabilities of turbulence modelling approaches available in CFD methods to model complex aerodynamic flows at high Reynolds number. 21 partners focused on a restricted set of CFD approaches: Differential Reynolds Stress Models (DRSMs), advanced Unsteady RANS models, Scale-Adaptive Simulation (SAS), Wall Modelled LES and different hybrid RANS-LES coupling schemes. Basic URANS models show indeed their limits in the case of complex situations such as stall, detached flows, high-lift applications, swirling flows, buffet, etc.

The tandem of two inline cylinders have been selected as one of the test cases handled for this project. The averaged and unsteady characteristics of the flow, in the flow and at the surface of the two cylinders, had previously been studied in a series of experiments performed in NASA Langley Research Center leading to a detailed set of data.

This configuration is a model for interaction problems commonly encountered in airframe noise configurations (e.g. hydraulic lines, support and hoses on a landing gear, Fig. 2.1). It involves many complex flow phenomena: separation of turbulent boundary layer and free shear layer roll-up, interaction of unsteady wake of the front cylinder with the downstream one, unsteady massively separated flow in the wake of the rear cylinder, etc. In this context, in a “noise-prediction” orientation of the numerical study in particular, conventional unsteady RANS approaches are not applicable and the capability of the aforementioned numerical methods to accurately reproduce the flow and predict noise have been investigated during the ATAAC project.

The flow around a single cylinder and the wake past of it have been well investigated at moderate and high Reynolds numbers, experimentally (e.g. [Roshko, 1954](#); [Williamson, 1992](#); [Perrin et al., 2007](#)) and numerically (e.g. [Braza et al., 1986](#); [Persillon and Braza, 1998](#); [Braza et al., 2001](#)), identifying several flow regimes as a function of the Reynolds number. The flow is laminar up to $Re \approx 200$, with two symmetrical recirculation vortices just downstream the cylinder. From $Re \approx 40$, the symmetry is broken due to the stream perturbations and the counter rotating vortices are alternatively detached and convected in the flow. This two-dimensional phenomenon generates a series of vortices called the von Kármán street. The vortices are detached periodically and the corresponding frequency of the detachment



Figure 2.1: Main landing gear of a Cessna 404 Titan.

is non dimensionalised to give the Strouhal number:

$$St = \frac{f_{VK} D}{U_\infty} \quad (2.1)$$

where f_{VK} is the frequency of the vortices detachment (two successive detachments of the counter-rotating vortices is one period of the phenomenon), D the diameter of the cylinder (or the characteristic length of the body) and U_∞ the freestream velocity of the flow. The Strouhal number depends on the body shape and the Reynolds number. This periodical detachment is characterised by a time evolution of the aerodynamic forces applying on the body at f_{VK} for the perpendicular ones (lift) and $f_{VK}/2$ for the streamwise ones (drag). Close to $Re \approx 200$, three-dimensional effects can be observed: the von Kármán vortices undulate in the crosswise direction, parallel to the cylinder, with a wavelength of about $4D$. For Reynolds numbers higher than 200, this wavelength is reduced to $1D$ and first turbulence phenomena develop in the wake. The flow is fully turbulent for $Re > 300$ which is the case in this study, as the Reynolds number equals to 166,000 as detailed in the next section.

A first synthesis of numerical simulations carried out for this test case was carried out by Lockhard, regrouping 13 contributions involving different modelling approaches, as well as previous simulations by [Khorrami et al. \(2007\)](#), using URANS SST. These simulations indicated that the majority of the approaches captured quite well the Strouhal number of the vortex shedding frequency around the first cylinder, ($St = 0.24$). Furthermore, as is seen in the ATAAC European program, the DES approaches better capture the complex vortex dynamics of the present flow, especially the formation of Kelvin-Helmholtz vortices in the separated shear layers. In the experimental context, it was found that the shear layers formed downstream of the first cylinder wrap around the second cylinder and interact non-linearly with the complex turbulence background, producing predominant frequencies in the energy spectrum, in the range of acoustic noise. Moreover, the numerical studies reported by Lockard in the context of the workshop for airframe noise computation, evaluated the mean drag coefficient provided by the different simulations, that had shown quite a dispersion among the different studies, with a most probable mean value of order 0.484 around the first cylinder.

2.1.2 Test-case description

Three series of experiments have been carried out on this geometry. The first set was conducted in the subsonic, atmospheric NASA-Langley Basic Aerodynamics Research Tunnel (BART; Fig. 2.2), and aimed at analysing the overall flow properties around the cylinders, by means of Particle Image Velocimetry (PIV) and hot-wire measurements (phase 1 of BART experiments, [Jenkins et al., 2005](#)). The second set of experiments was conducted in the same wind tunnel and aimed at measuring detailed average and unsteady pressure distribution at the surface of the cylinder, using static pressure orifices and piezoresistive, differential pressure transducers on the two cylin-



Figure 2.2: Experimental set-up.

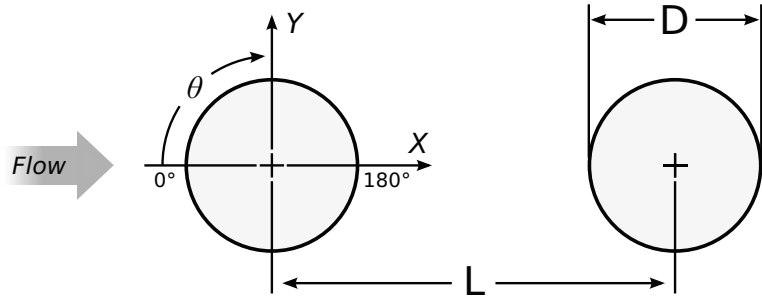


Figure 2.3: Diagram of the cylinders tandem and coordinate reference system.

ders (phase 2, Jenkins et al., 2006). The cylinders diameter has been slightly increased for this study to accommodate the pressure tubing and electrical wiring, but flow velocity has been adapted to keep the same Reynolds number, 1.66×10^5 . The freestream turbulence level measured in this wind tunnel was less than 0.10%. Finally, the acoustic environment of this configuration have been studied in the Quiet Flow Facility (QFF) at NASA Langley (Lockard et al., 2007). While the QFF is an open jet facility specifically designed for anechoic testing, the flow has been adapted to obtain the same shedding frequency as in the BART experiments. All the facility dimensions and the flow properties are summarised in Table 2.1, in the next section presenting the numerical method. To ensure a fully turbulent shedding process, the boundary layers on the upstream cylinder were tripped between azimuthal locations of 50 and 60 degrees and -50 and -60 degrees

2.1.3 Numerical method

This study has been carried out by using the Navier-Stokes Multiblock (NSMB) solver. The main properties of this code have been presented in Szubert et al. (2015b), among other articles. This article details a major part of the work achieved during this Ph.D. study and has been included in this manuscript in subsection 3.1.1 of chapter 3, page 52. The reader is invited to read the section of this article dedicated to the NSMB code.

In the context of the ATAAC programme, the numerical study has been performed with non-dimensional parameters. The velocity, the density, the temperature and the cylinders diameter have been set to the unity. This leads to the value of 43.2579 for the static pressure P and the gas constant:

$$P = \rho RT, \quad a = \sqrt{\gamma_{\text{air}} RT}, \quad M = \frac{U}{a} \quad (2.2)$$

Finally:

$$P = R = \frac{1}{M^2 \gamma_{\text{air}}} \quad (2.3)$$

The time has also been non-dimentionalised as follows: $t^* = t U_\infty / D$.

The main numerical and experimental parameters can be compared in Table 2.1. H/D is the non-dimensionalised height or span of the cylinders, and W/D is the non-dimensionalised width of the wind tunnel in the test section.

	BART		QFF	CFD
	<i>Phase 1</i>	<i>Phase 2</i>		
D	0.04445 m	0.05715 m	0.05715 m	1
L/D			3.7	
H/D	16.0	12.4	16.0	3
W/D	22.9	17.8	10.7	17.8
Mach	0.1635	0.1285	0.1274	0.1285
U_∞	56.0 m.s ⁻¹	44.0 m.s ⁻¹	43.4 m.s ⁻¹	1
Re			1.66×10^5	

Table 2.1: Experimental and numerical main parameters of the tandem cylinders geometry and flow

The 4th order skewsymmetric central scheme has been used for the space discretisation. Implicit time integration using the dual time stepping technique with 3 Gauss-Seidel iterations has been performed. Since NSMB solves the compressible Navier-Stokes and models equations, the preconditioning of [Weiss and Smith \(1995\)](#) is used to solve the flow at the Mach number 0.1285. This choice has been validated by [Marcel \(2011\)](#) for a Mach 0.18 flow through a confined bundle of cylinders by using the same CFD code.

The grid has been provided by the NTS (New Technologies and Services) partner from Saint Petersburg, Russia, in the context of the ATAAC programme. The grid is divided in 16 blocks of the parallel computation, and have approximately 156,000 volume cells. The gridlines are shown in Fig. 2.4 for the whole domain and around the two cylinders. The grid is slightly refined around the downstream cylinder has more turbulence is expected. The non-dimensionnalized first-cell height around this cylinder is 3.4×10^{-5} while it is 5×10^{-5} for the upstream one. The total length of the domain is $44D$.

On the solid wall, impermeability and no-slip conditions are employed. The far-field conditions are characteristic variables with extrapolation in time. The upstream turbulence intensity is set to $TU = 0.08\%$.

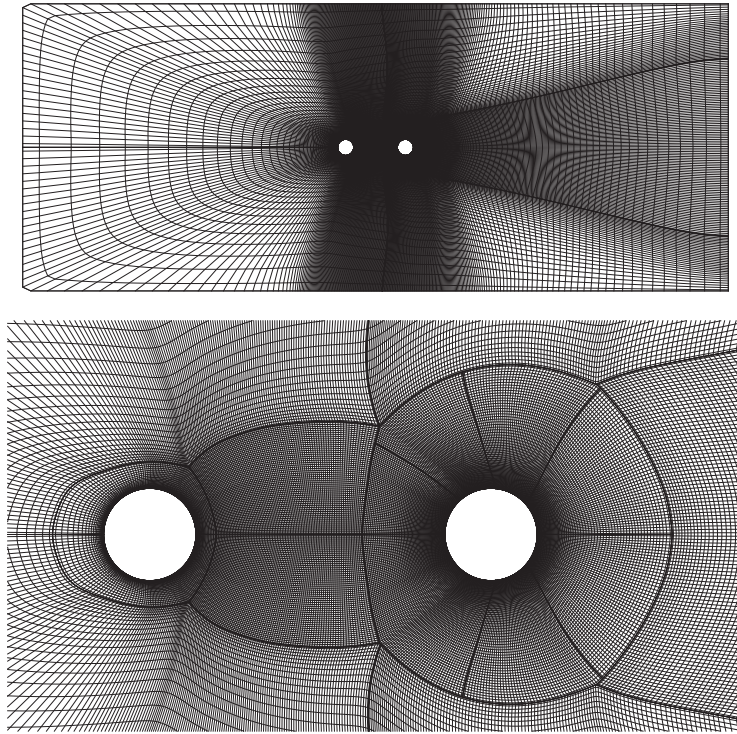


Figure 2.4: Multiblock domain of the tandem of cylinders.

2.1.4 Results

2.1.4.1 Flow overview

Eight snapshots of the vorticity field from a preliminary $k-\omega$ -SST simulation covering one period of the von Kármán phenomenon can be observed in Fig. 2.5. The main characteristic of the field is that the vortex shedding occurs at the same frequency for the two cylinders, due to the wake of the first cylinder that intensively influences the generation of vortices by the second cylinder. The distance $L/D = 3.7$ between the two cylinder is optimal to observe this phenomenon. In case of a smaller or a bigger distance, the vortex shedding would be in phase opposition between the two cylinders, generating a more complexe wake downstream the whole geometry. After this preliminary overview of the flow structure, a numerical study is carried out in order to determine the best convergence criterion and turbulence models to simulate this test case. These parameters don't change the overall flow structure and the above description remains valid.

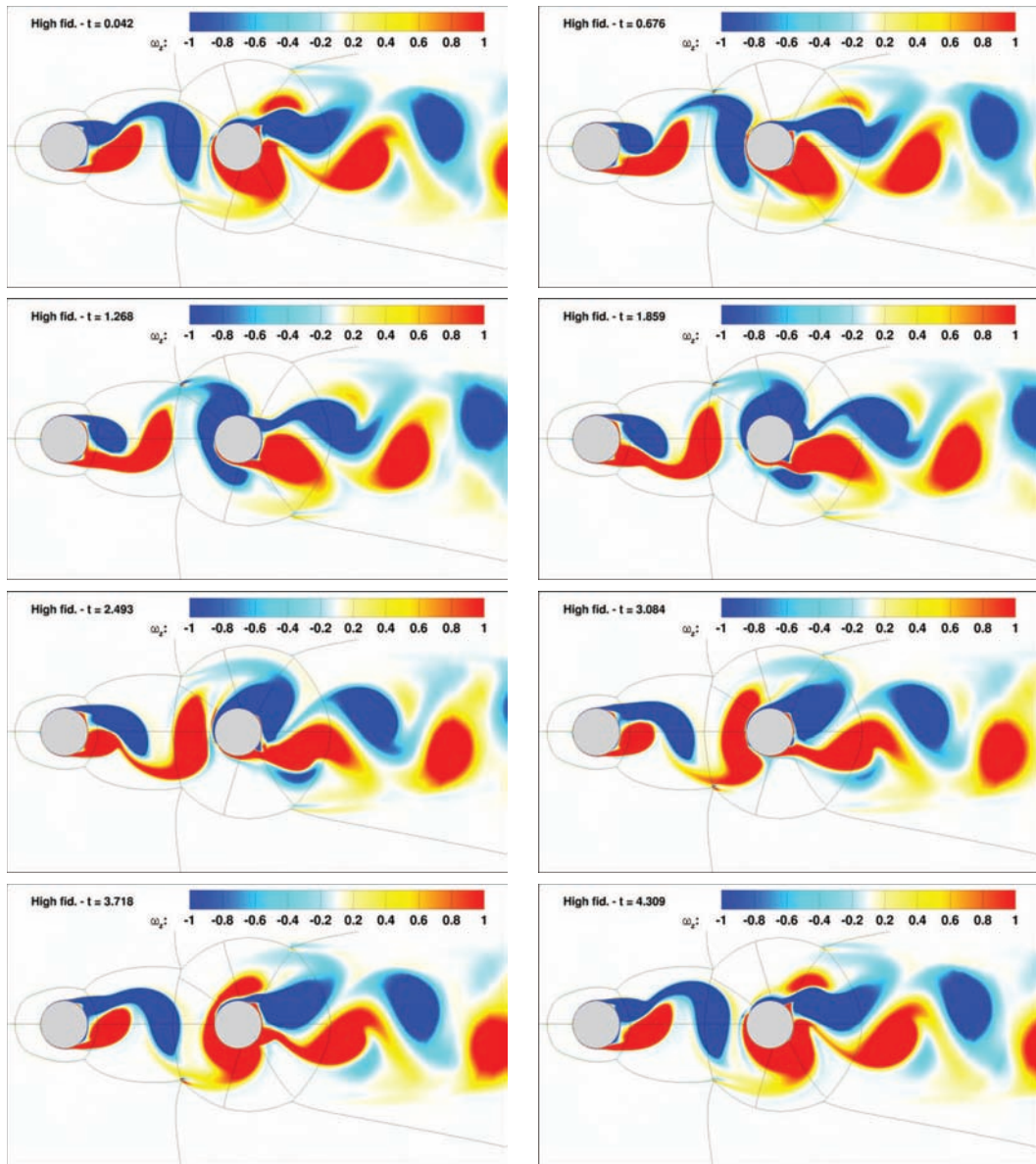


Figure 2.5: Snapshots of the vorticity field by k - ω -SST simulation covering one period of von Kármán.

2.1.4.2 Convergence study

In the context of the dual-time stepping, a sensitivity study of the physical results regarding the tolerance of the convergence criterion is first carried out. The convergence criterion at the inner step n is defined by the ratio between the L_2 -norm of the density equation residual at the inner step n and the one at the initial inner step. It is calculated at each inner computation step and when the tolerance is reached, the physical solution is saved at the current physical time step and the process goes on at the next outerstep. The system of equations needs to converge enough to provide a good prediction of the physical solution. However, a very low tolerance implies long computation time to reach the requested value and becomes useless compared to the numerical uncertainties (time and grid resolutions, computer precision). This study is performed to determine the better tolerance for the three-dimensional computations.

For this study, the $k-\omega$ -SST model of [Menter \(1994\)](#) (see also section A.2.3.2 of appendix A, page 141) is used, as it is well designed for flows under high pressure gradient, and the non-dimensionalised time step $\Delta t^* = 0.00845$ has been chosen from the ATAAC programme.

The RMS value of the lift and drag coefficient fluctuations of the two cylinders are calculated at each outerstep. The last steps are plotted in Fig. 2.6 for the three tolerance values analysed. The curves trend shows at first glance that the difference between the two smaller tolerances is less than between 10^{-3} and 10^{-5} . While the physical solutions were well converged, small oscillations are visible in the RMS values and are due to numerical resolution.

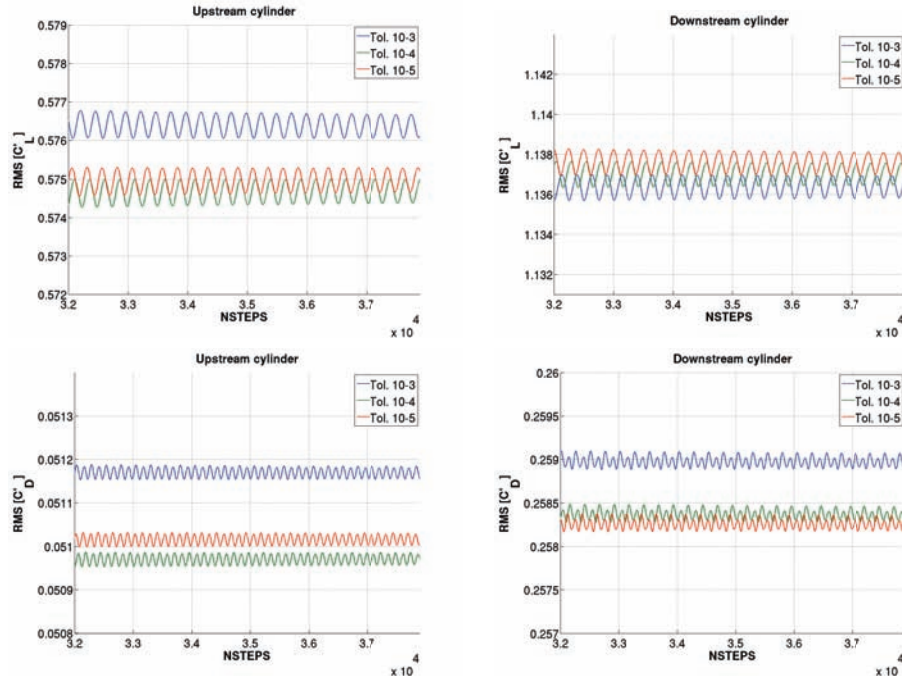


Figure 2.6: Evolution of the RMS values of the lift and drag coefficients fluctuations for three convergence tolerances.

The final values of the RMS, as well as the mean of the lift and drag coefficients, are reported in Table 2.2 for a quantitative comparison. The three tolerances give

Tol.	Upstream cylinder				Downstream cylinder			
	$\overline{C_D}$	$\overline{C_L}$	RMS(C'_L)	RMS(C'_D)	$\overline{C_D}$	$\overline{C_L}$	RMS(C'_L)	RMS(C'_D)
10^{-3}	0.7997	0.0022	0.0512	0.5765	0.2035	-0.0020	0.2590	1.1363
10^{-4}	0.7990	0.0028	0.0509	0.5746	0.2047	-0.0036	0.2584	1.1370
10^{-5}	0.7991	0.0027	0.0510	0.5749	0.2045	-0.0049	0.2583	1.1377

Table 2.2: Mean values of the lift and drag coefficients and RMS values of their fluctuations for the two cylinders.

very close results with a difference < 1%, except for the mean lift value on both cylinders. Between 10^{-3} and 10^{-4} , $\overline{C_L}$ is increased by 20% on the first cylinder and 44% on the second one, while between 10^{-4} and 10^{-5} , $\overline{C_L}$ is 4% smaller on the upstream cylinder, and 27% higher on the downstream one. In the spirit of getting meaningful physical results in a reasonable computation time, the tolerance 10^{-4} is retained for the remaining simulations.

2.1.4.3 Turbulence model study

A similar comparison is carried out to compare the results of four turbulence models. The mean and RMS values of the lift and drag coefficient time evolution are reported in Table 2.3. The [Edwards and Chandra \(1996\)](#) modified [Spalart and Allmaras \(1994\)](#) (see also section A.1.1 of appendix A, page 135) and the $k-\omega$ -SST ([Menter, 1994](#) and section A.2.3.2 page 141) give very close results in mean and amplitude. The $k-\omega$ -BSL ([Menter, 1994](#) and section A.2.3.1 page 139) is more dissipative and as a consequence, the amplitude of the aerodynamic coefficients are smaller.

Models	Upstream cylinder				Downstream cylinder			
	$\overline{C_D}$	$\overline{C_L}$	RMS(C'_L)	RMS(C'_D)	$\overline{C_D}$	$\overline{C_L}$	RMS(C'_L)	RMS(C'_D)
SA-E	0.7826	0.0028	0.0742	0.6246	0.2008	0.0018	0.3068	1.3295
$k-\omega$ -SST	0.7990	0.0028	0.0509	0.5746	0.2047	-0.0036	0.2581	1.1370
$k-\omega$ -BSL	0.5567	0.0011	0.0167	0.2523	0.2852	-0.0054	0.1246	0.8045

Table 2.3: Mean values of the lift and drag coefficients and RMS values of their fluctuations for three turbulence models.

The mean streamlines in the wake of each cylinder are plotted for the three turbulence models in Fig. 2.7. The overall prediction of the flow is similar between the three models and the experiment (Fig. 2.8) and the symmetry between the upper and lower sides of the flow is observed. However, they predict slight different size of the recirculation area, in particular none of them matches the experimental measurements.

The non-dimensionalised streamwise velocity at $y = 0$ measured in the wake of the two cylinders is plotted in Fig. 2.9, and the recirculation lengths ($x \wedge U(x) = 0$) are reported in Table 2.4. In the BART experiment, the second recirculation has been reduced by 80% compared to the first. This difference might be due to the position of the cylinders compared to each other. The velocity in the wake of the

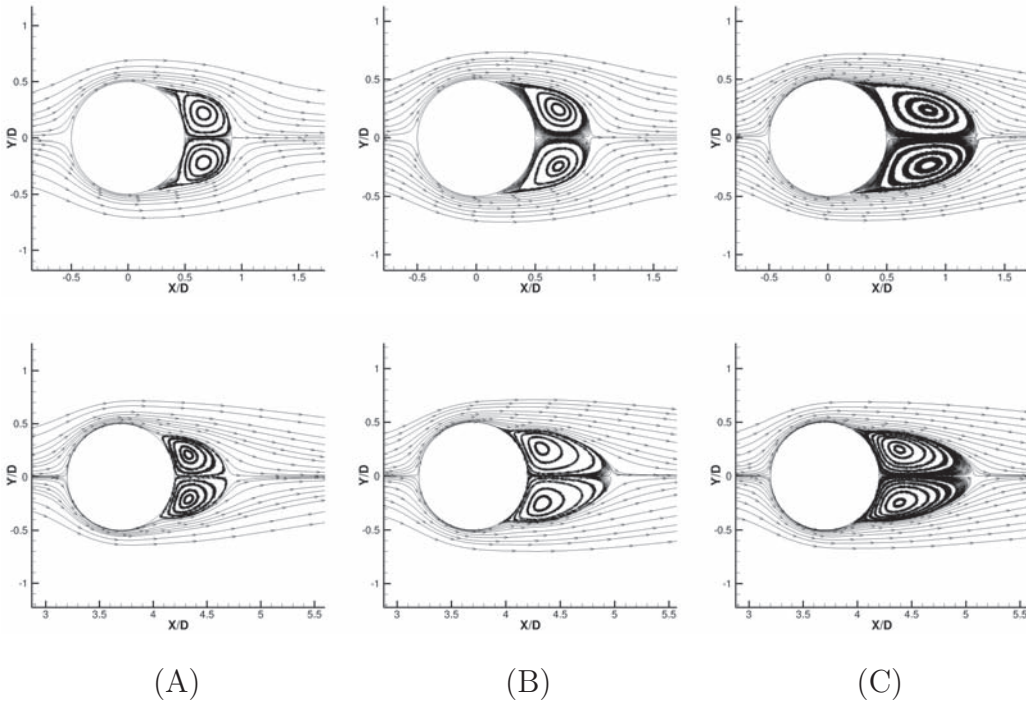


Figure 2.7: Comparison of the mean streamlines in the wake of the upstream (top) and the downstream (bottom) cylinders. (A) SA-E, (B) k - ω -SST, (C) k - ω -BSL.

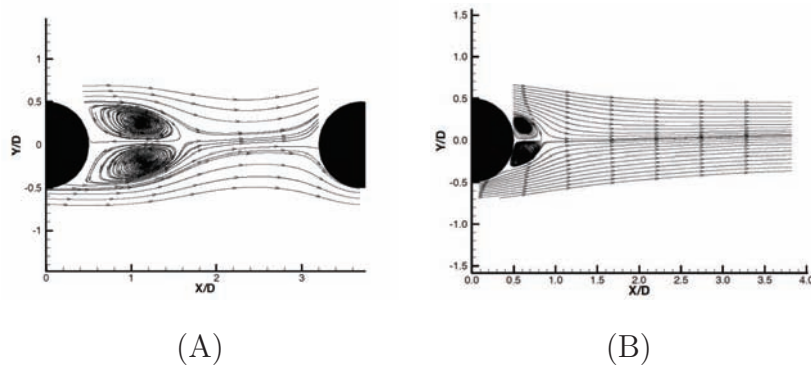


Figure 2.8: Mean stream lines from PIV measurements. (A) Upstream cylinder, (B) Downstream cylinder ([Jenkins et al., 2005](#)).

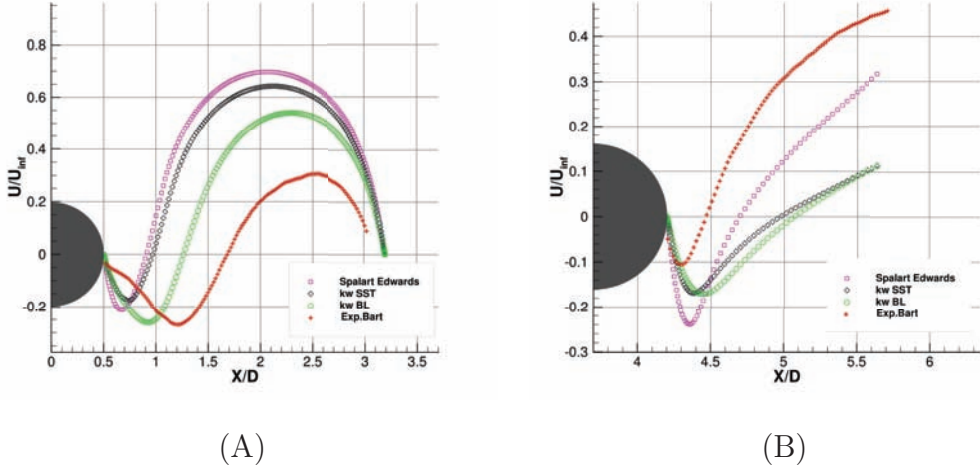


Figure 2.9: Comparison between turbulence models en experiment of normalised streamwise velocity in the wake. (A) Upstream cylinder, (B) Downstream cylinder.

first cylinder is limited by the presence of the second cylinder and this favours the development of the vortices before they detach, while this is not the case for the second cylinder. However, this phenomenon is not observed in the simulations, which give an opposite trend, and the difference between the two regions is less important (SA-E and $k-\omega$ -SST: +20%, $k-\omega$ -SST: +67%).

Models/Source	L_{recirc}/D	
	Upstream cyl.	Downstream cyl.
PIV (Jenkins et al., 2005)	1.2	0.25
SA-E	0.4	0.5
$k-\omega$ -SST	0.45	0.75
$k-\omega$ -BL	0.75	0.9

Table 2.4: Recirculation length downstream each cylinder.

Spectral analysis

A spectral analysis is carried out on the time evolution of the lift and drag coefficients recorded at a physical time step $\Delta t^* = 0.00845$, the same as the simulation itself. All signals are 17751 sample length, and are processed by the Welch's method ([Welch, 1967](#)) with the following parameters:

- Window: Hanning,
- Window size: $N_{wind} = 8192$ samples,
- Overlap: 65%,

- Zero padding: $N_{FFT} = 2^{18} = 262144$.

These parameters give the following resolutions:

- $\Delta f \approx 4.5 \times 10^{-4}$ Hz,
- $B \approx 5.8 \times 10^{-2}$ Hz.

where $\Delta f = 1/(\Delta t^* N_{FFT})$ is directly related to the signal points available, and $B = \alpha/(N_{wind}\Delta t^*)$ is the dynamic resolution given by the window definition and parameters (among which α). The spectra of the lift coefficient, for the two cylinders, are plotted in Fig. 2.10. The major peak is identified as well as few harmonics. As can be noticed, the frequency content is very similar between the two cylinders and the main frequencies appears for both. The main peak is identified to the Strouhal number. Indeed, the lift evolution is the same as the vortex shedding: it is maximum when a vortex detaches on the upper side of the cylinder, minimum when a vortex detaches on its lower side. Due to the symmetry in the streamwise direction, the drag gives twice this frequency (Fig. 2.11): it is maximum just before each vortex detachment. The Strouhal numbers are reported in Table 2.5 and are compared to the experimental value. The $k-\omega$ -BSL model predicts the exact frequency of the vortex shedding while the other models are closed to 0.241 (SA-E: +1%, $k-\omega$ -SST: -3%).

Models/Source	Strouhal ($St = f_{VK}D/U_\infty$)
PIV (Jenkins et al., 2005)	0.241
SA-E	0.244
$k-\omega$ -SST	0.234
$k-\omega$ -BSL	0.241

Table 2.5: Comparison of Strouhal numbers.

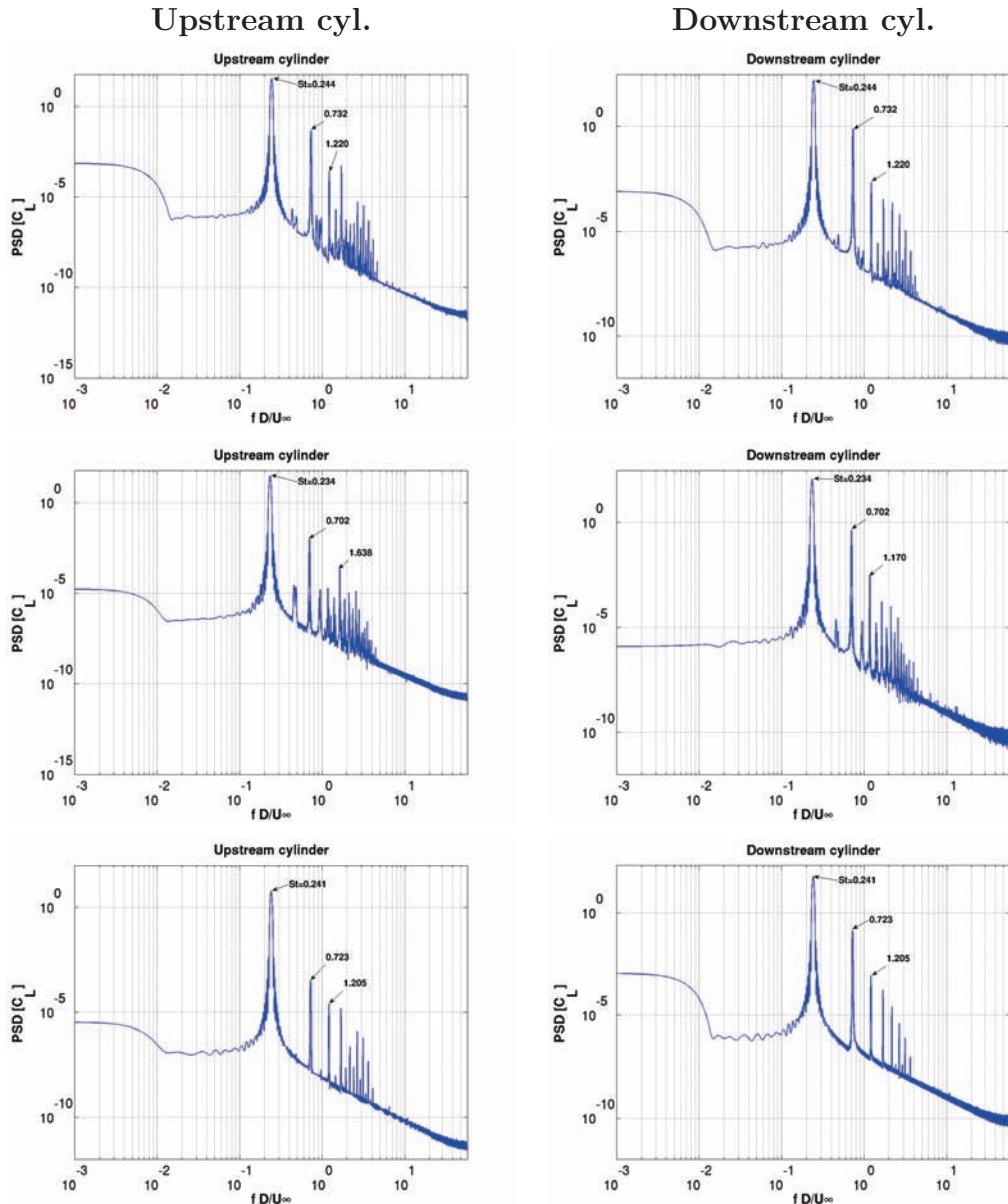


Figure 2.10: PSD of the lift coefficient time evolution for the two cylinders. Top: SA, middle: $k-\omega$ -SST, bottom: $k-\omega$ -BSL.

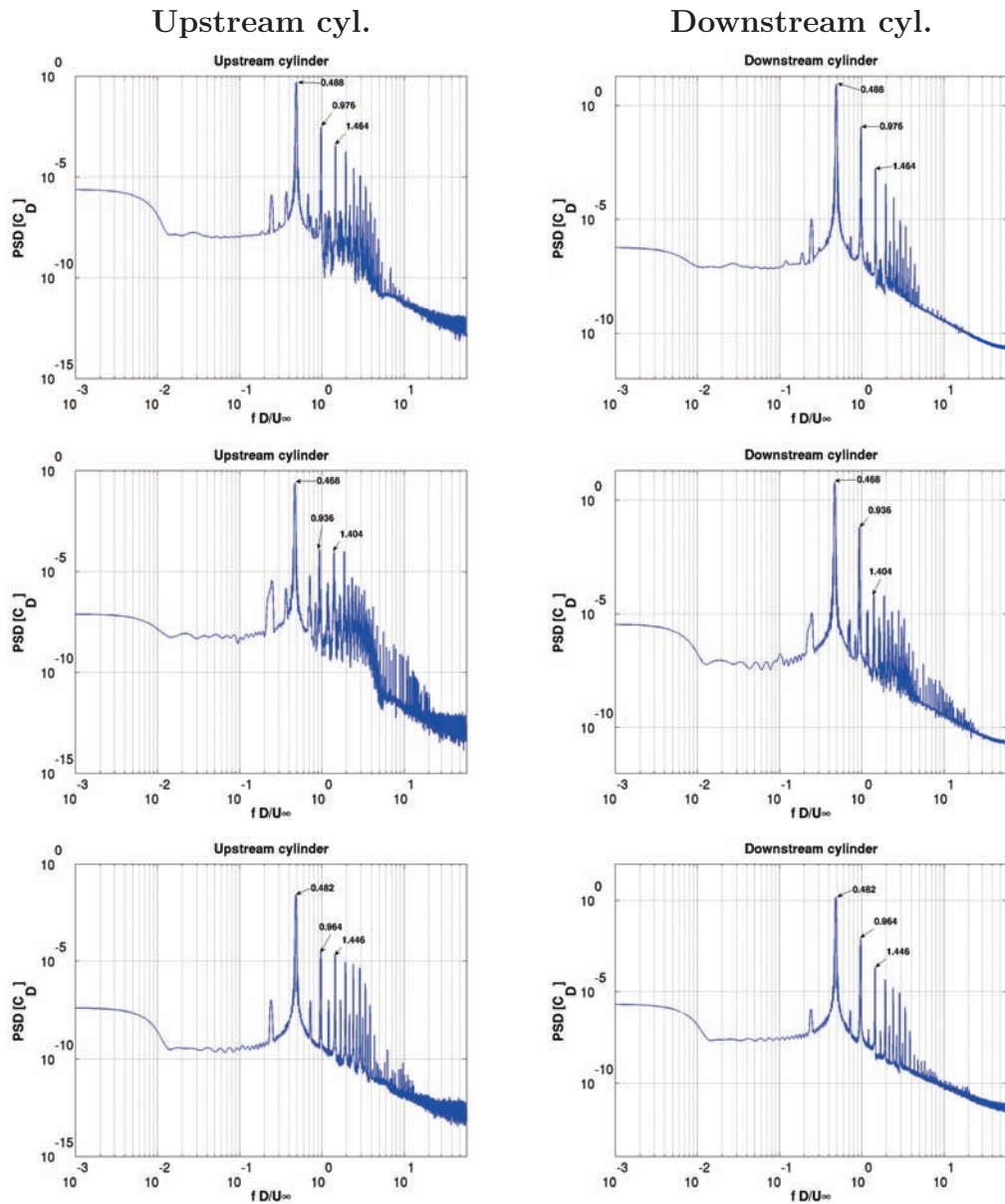


Figure 2.11: PSD of the **drag** coefficient time evolution for the two cylinders.
Top: SA, middle: k - ω -SST, bottom: k - ω -BSL.

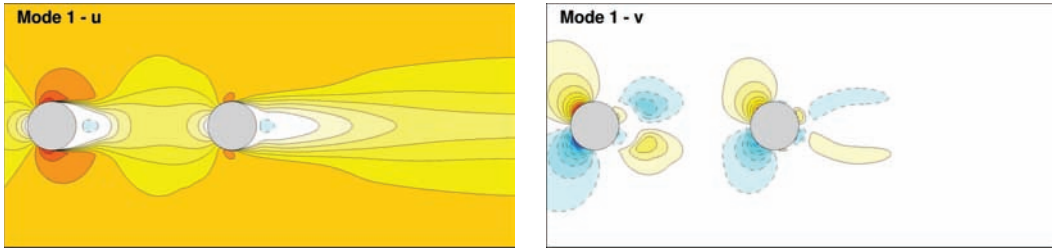


Figure 2.12: First POD mode of the streamwise (left) and crosswise (right) velocity components.

2.1.4.4 POD analysis

The Proper Orthogonal Decomposition (POD) is a mathematical technique used to analyze complex physical systems of a great number of degrees of freedom, allowing to represent these systems in an optimal way. This method is applied in a wide range of scientific fields such that signal and image processing, chemistry, medicine, oceanography, meteorology. In the context of the fluid dynamics, this method has been introduced by (Lumley, 1967) to analyse the coherent structures in a turbulent flow, which are usually of high energy, the lowest energy range corresponding to the random fluctuations. The current POD analysis is carried out based on the ‘separable POD’ (Holmes et al., 1996). The objective is to find an approximation of the physical flow as follows:

$$\mathbf{U}(\mathbf{x}, t) = \bar{\mathbf{U}}(\mathbf{x}) + \mathbf{u}(\mathbf{x}, t) = \bar{\mathbf{U}}(\mathbf{x}) + \sum_{n=2}^{N_{\text{POD}}} a_n(t) \phi_n(\mathbf{x}), \quad (2.4)$$

where $\phi_n(\mathbf{x})$ are the shape (spatial) functions and $a_n(t)$ are the associated temporal coefficients. In the context of this study, the ‘snapshot POD’ (Sirovich, 1987; Aubry et al., 1991) is used to determine the temporal coefficients from the time correlations arising from the snapshots generated during the simulation. The spatial modes are determined by projecting the physical field on these temporal coefficients. A Fortran code developed in our research group has been used to read the data, calculate the temporal coefficients and spatial modes and write results. Here, 1132 snapshots of the streamwise and crosswise velocity components, generated from a $k-\omega$ -SST simulation every $t^* = 0.04225$, 5 times the simulation time step, are used covering 10 periods of vortex shedding. The first POD mode corresponds to the mean field as it is included in the original database (Fig. 2.12). Shape functions from modes 2 to 6 are plotted in Fig. 2.13, and are clearly identified to the von Kármán phenomenon, giving sub-spatial frequencies as the mode order increases. Shape functions of the next 5 modes are plotted in Fig. 2.14. They confirm the tendency of the subdivision of the spatial modes structures as their range increases. Moreover, the higher shape values move from the vortex shedding area to the shear-layer one, characterised by Kelvin-Helmholtz vortices. The tendency is confirmed at higher-range modes (Fig. 2.15).

The time evolution of the temporal coefficients are plotted in the Fig. 2.16 and 2.17. For the first mode, the constant time evolution confirms the property of the first mode which represents the mean field. Other modes are associated two by two, corresponding to two different phases, similarly to the shape functions, and

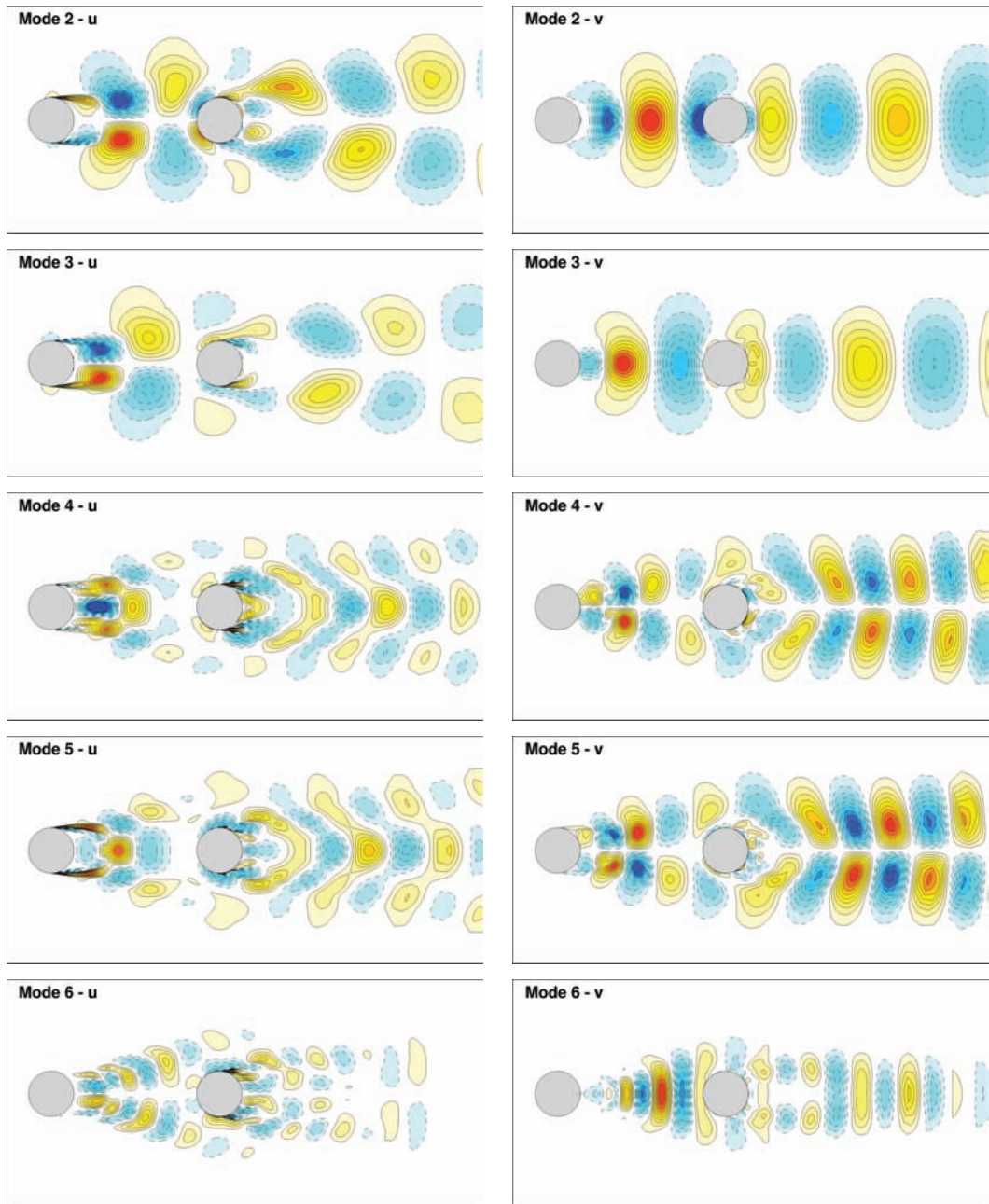


Figure 2.13: POD modes 2 to 6 of the streamwise (left) and crosswise (right) velocity components.

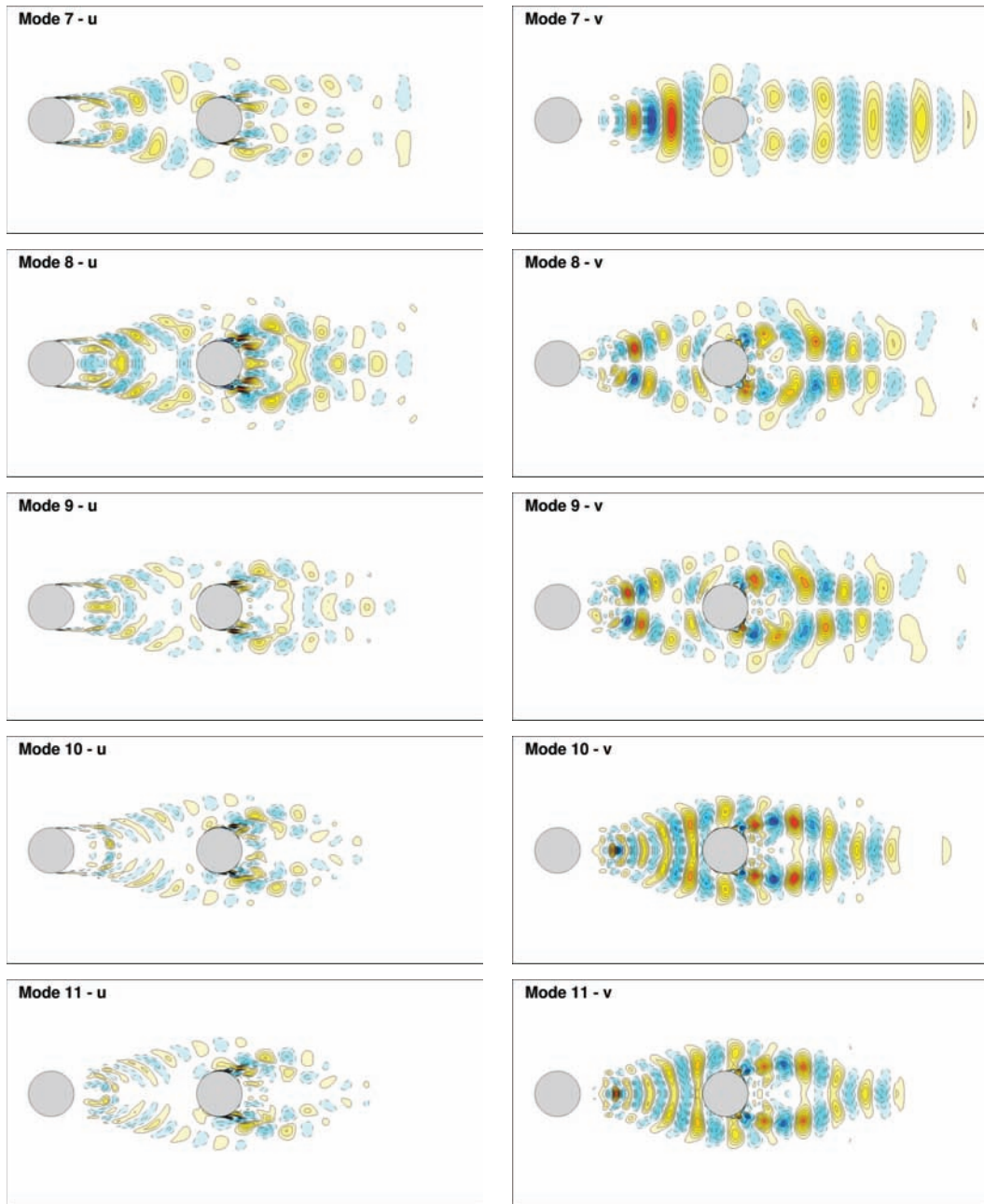


Figure 2.14: POD modes 7 to 11 of the streamwise (left) and crosswise (right) velocity components.

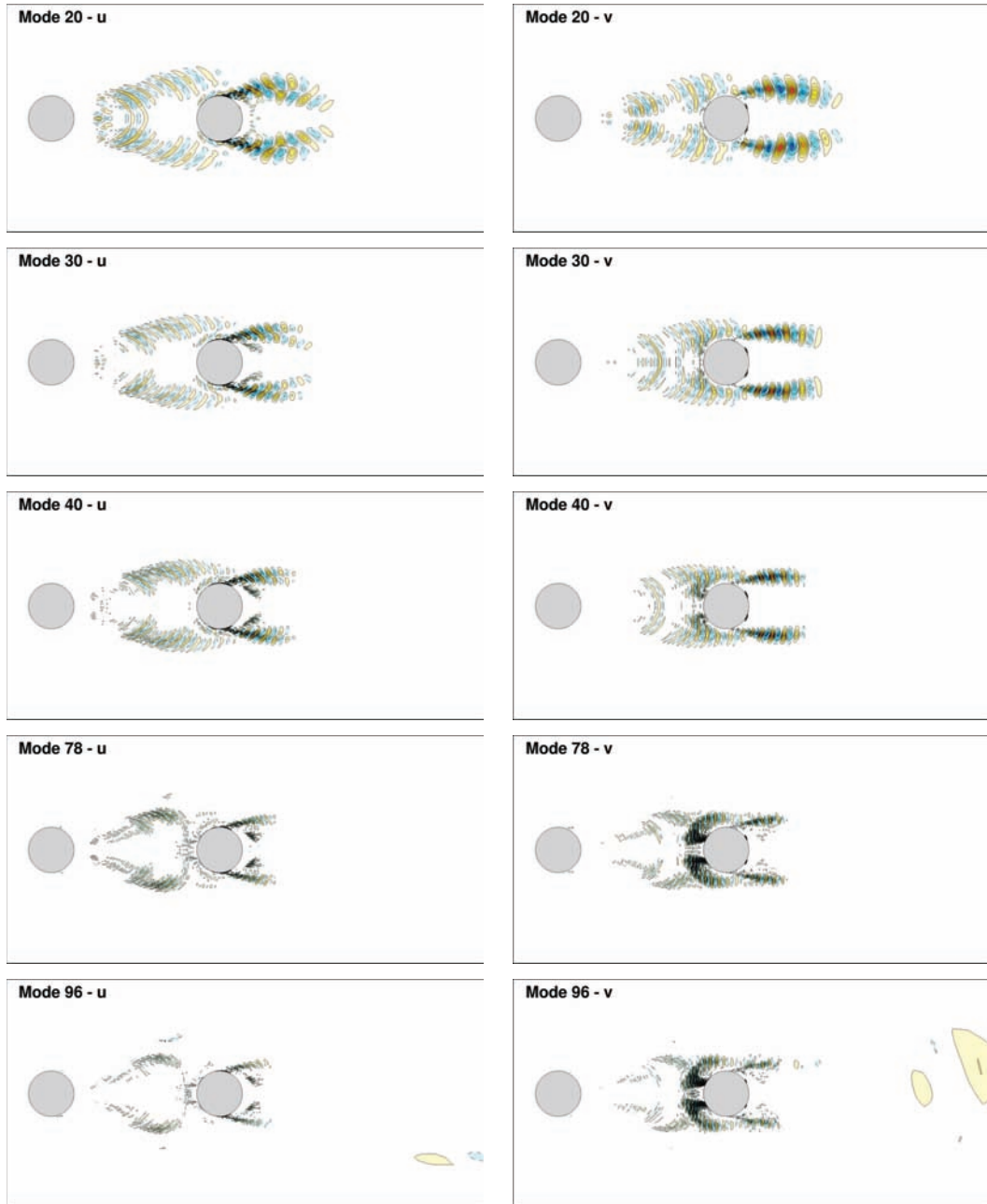


Figure 2.15: Higher-range POD modes of the streamwise (right) and crosswise (left) velocity components.

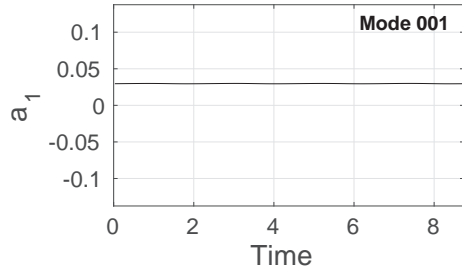


Figure 2.16: Temporal coefficient time evolution of first POD mode.

are periodical. This illustrates the link between the POD and the Fourier Series Expansion. The flow itself is very periodical and statistically quasi-stationary. The POD temporal coefficients corresponds to an harmonic decomposition on the mode $\cos(2\pi kt/T)$ and $\sin(2\pi kt/T)$, with $k \geq 1$ and T the period of the physical phenomenon (Holmes et al., 1996). This explains the phase shift of the $\pi/2$ of the temporal signals and of the shape function (spatial translation) for each mode pair. Phase or Lissajous curves are plotted in Fig. 2.18 and show the periodicity of the signals (closed curves) as well as the increase of their frequency.

Spectra of the temporal coefficients are plotted in Fig. 2.19, as well as marks of harmonics of the main non-dimensionalised frequency of 0.231, and confirms the mode pair groups and the division of the main signals frequency by two from a pair to the next one.

Finally, the modes energy, related to the proper value found during the POD process, are plotted in the Fig. 2.20. It corresponds to the relative ‘information’ of the physical flow contained in each mode. The efficiency of the POD process is characterised by the accumulation of this information in the first modes. As the mean flow was included in the snapshots database, the first mode is the most energetic and contains 90% of the total information, and the next pair of modes represents 9% of the total energy, giving 99% of the flow field information contained in the first 3 modes, and 99.99% in the first 11 modes. Moreover, pair groups (modes 2-3, 4-5, etc...) are also visible in the energy distribution.

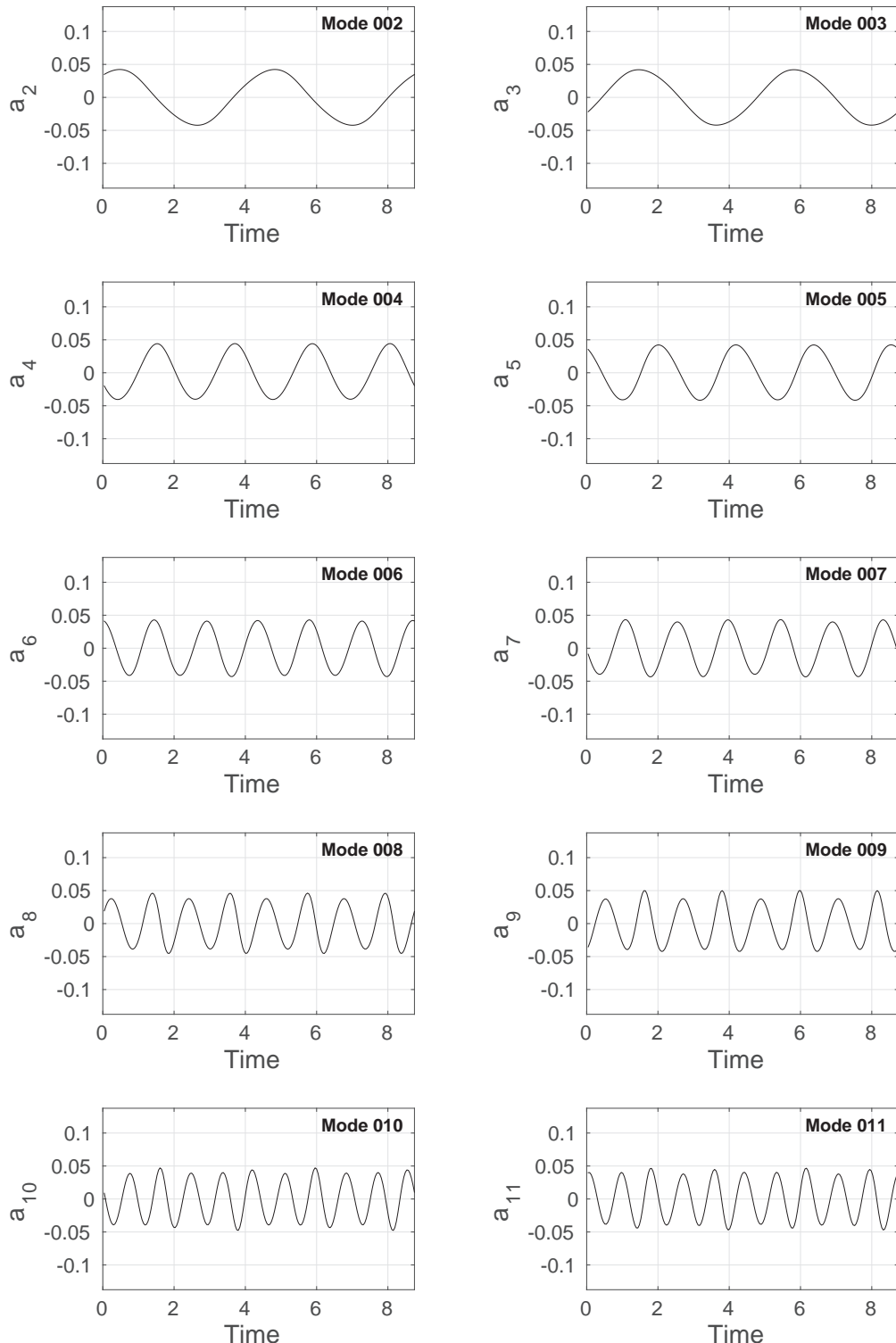


Figure 2.17: Temporal coefficient time evolution of POD modes 2 to 11.

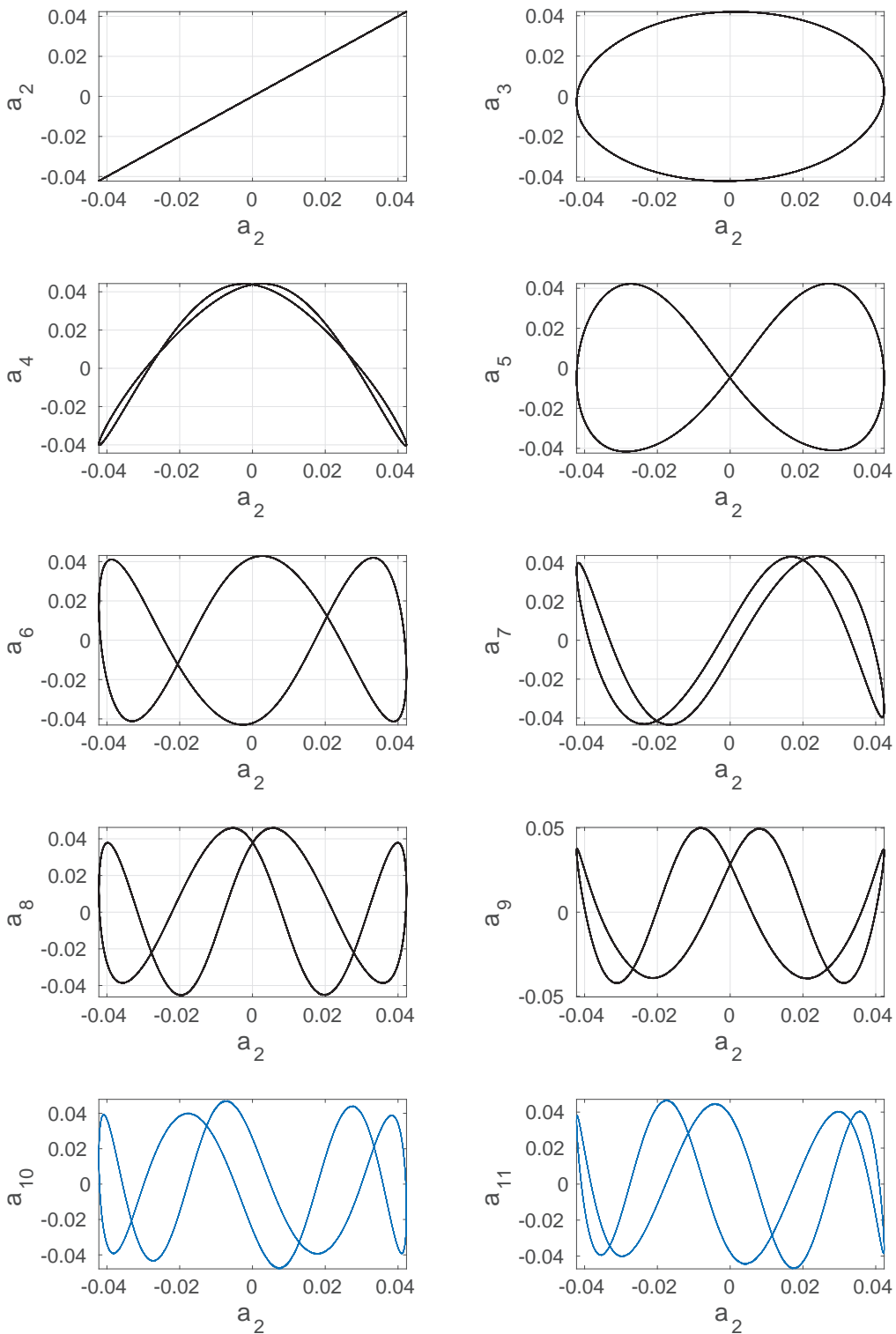


Figure 2.18: Lissajous curves associated to the temporal coefficients up to POD mode 11.

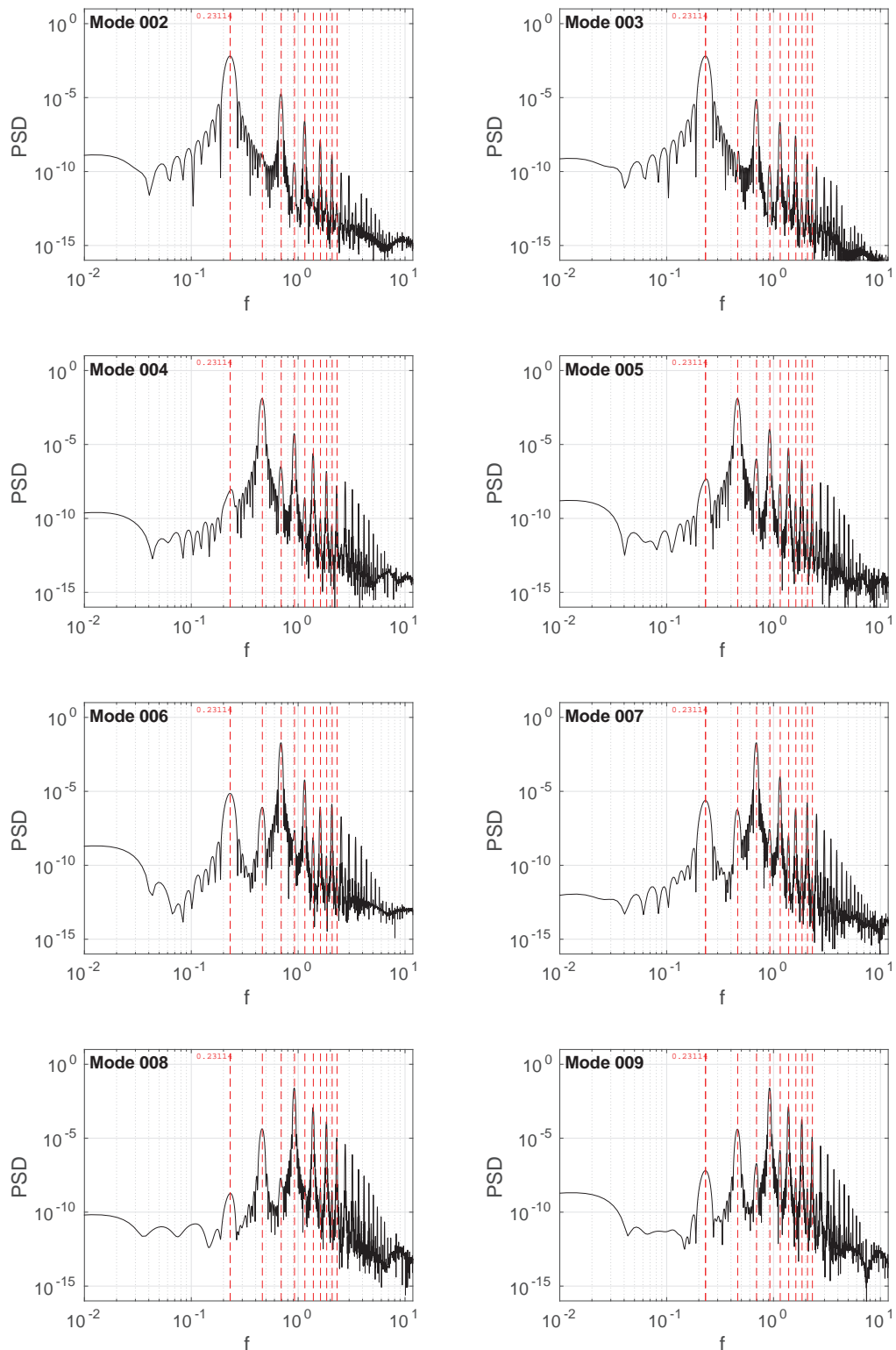


Figure 2.19: PSD associated to the temporal coefficients up to POD mode 9 (non-dimensionalised frequencies).

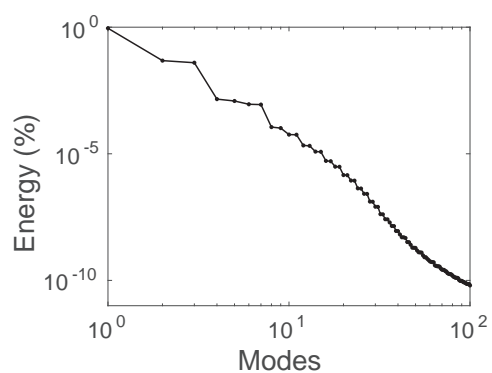


Figure 2.20: Energy distribution of the POD modes.

Reconstruction

The velocity fields are reconstructed from a limited number of POD modes using the relation 2.4 (here, $N_{\text{POD}} = 3, 5$ and 41). The vorticity is then calculated and compared to the original high-fidelity unprocessed field (snapshots form the simulation). They are plotted at $0 \times T_{VK}$ and $T_{VK}/4$ in Fig. 2.21, and $2T_{VK}/4$ (left) and $3T_{VK}/4$ in Fig. 2.21, T_{VK} being the period of the von Kármán vortex shedding. While their shapes are different from the orginal ones, the vortical structures are already reconstructed with only 3 modes (including the first mode). With 11 modes, their spatial expension is very close to the high-fidelity simulation. However, some spatial oscillation remains, in particular between the two cylinders. They disappear by adding more modes to the reconstruction (here, 30 more modes), where the vorticity field is almost qualitatively identical to the original one.

For a more detailed analysis of the reconstruction capabilities, the time evolution of the streamwise velocity component are recorded at 6 positions (Fig. 2.23). The signal from high-fidelity simulation is compared to reconstructions with 3, 5, 7 and 11 modes in Fig. 2.24, and with 11, 21 and 41 modes in Fig. 2.25. With only 3 modes, the overall periodicity of the signal is reproduced with a sinusoidal shape, but higher-frequency variations are not captured at all and more modes are needed, which is an expected result. While 99.99% of the flow information is contained in the first 11 modes as previously said, based on the proper values, some abrupt time variations of the flow are still not captured and up to 21 modes are necessary to reconstruct them (points 4 and 5 in particular). As said at the beginning of this subsection, the Proper Orthogonal Decomposition is used here to identify to most energetic modes inside a turbulent flow. The basis of the decomposition can also be used to build Reduced-Order Models (ROM) with a much more limited number of degrees of freedom than the URANS or other high-fidelity computations, allowing for faster computations. The capabilites and the speed of the ROM to model the fluid dynamics is directly related to the number of modes chosen to build the POD basis and thus the details one wants to model through the ROM. The reader can find an application of the ROM on an incompressible flow and a development of this method in the case of a compressible case in Bourguet (2008); Bourguet et al. (2011).

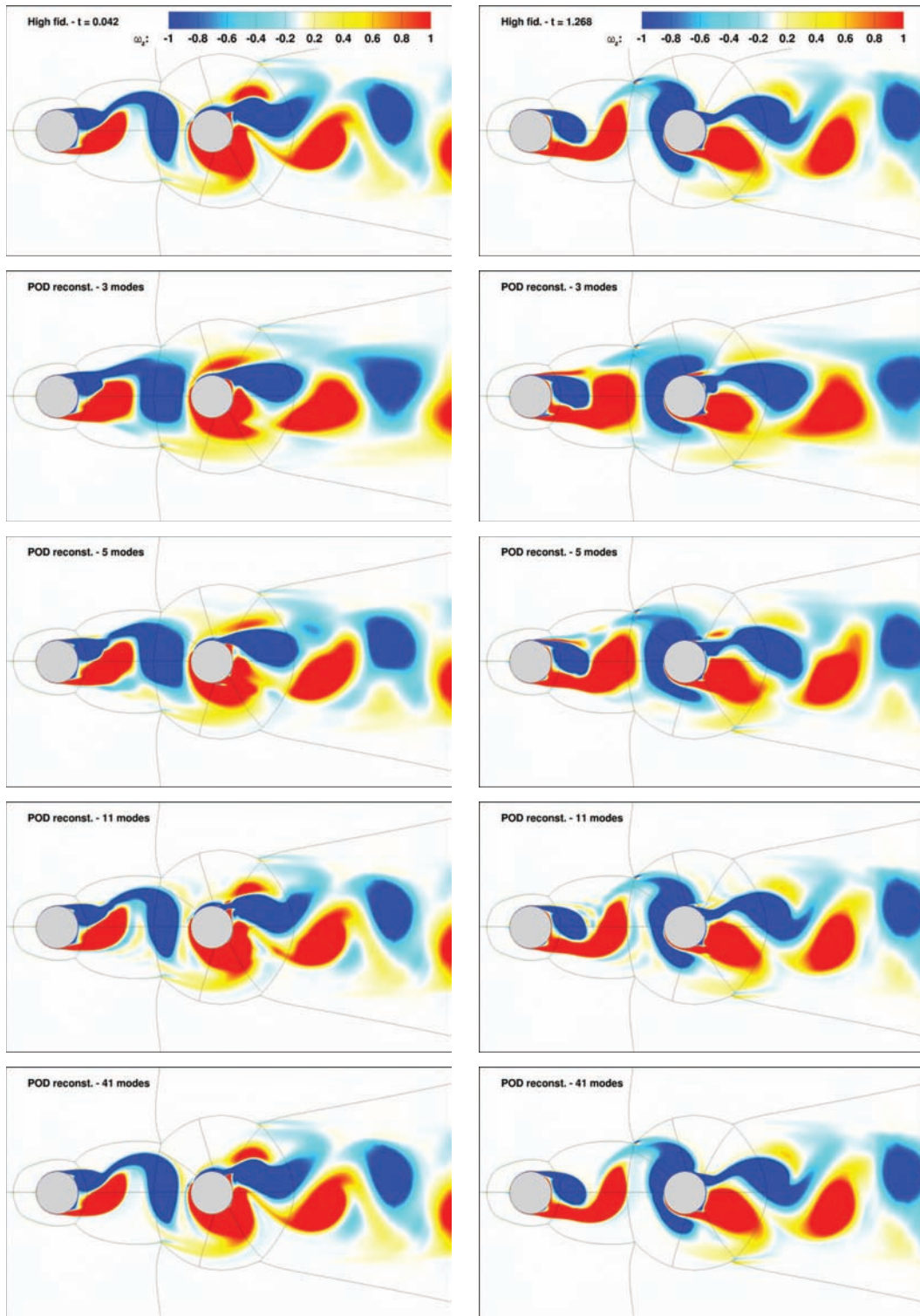


Figure 2.21: Vorticity field from URANS (top) and POD reconstruction from 3, 5 and 41 modes at $0 \times T_{VK}$ (left) and $T_{VK}/4$ (right) in static case.

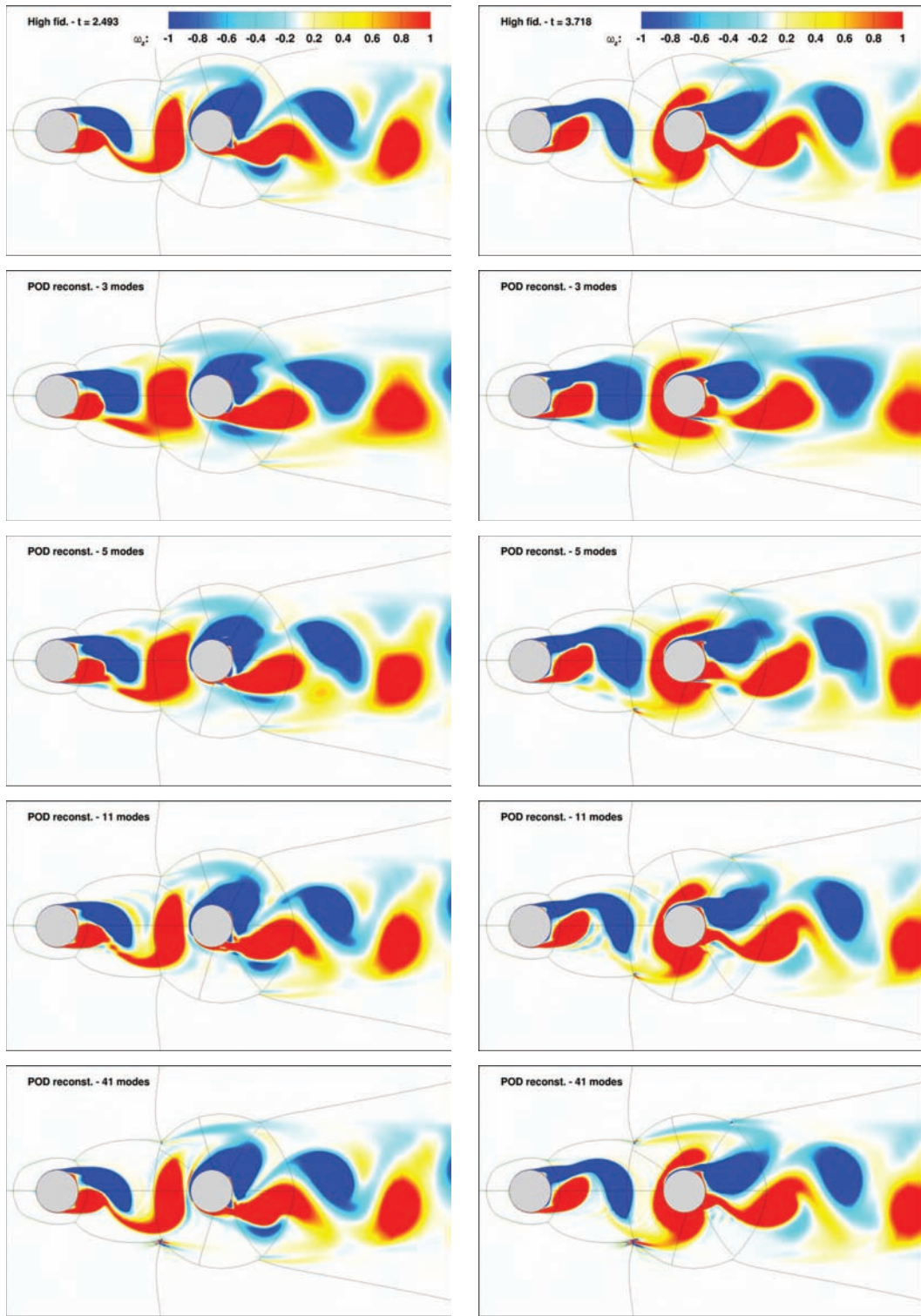


Figure 2.22: Vorticity field from URANS (top) and POD reconstruction from 3, 5 and 41 modes at $2T_{VK}/4$ (left) and $3T_{VK}/4$ (right) in static case.

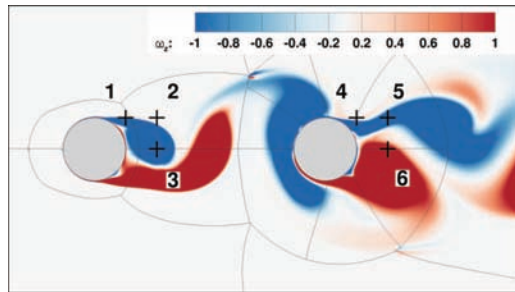


Figure 2.23: Monitoring locations for the reconstructed velocity analysis.

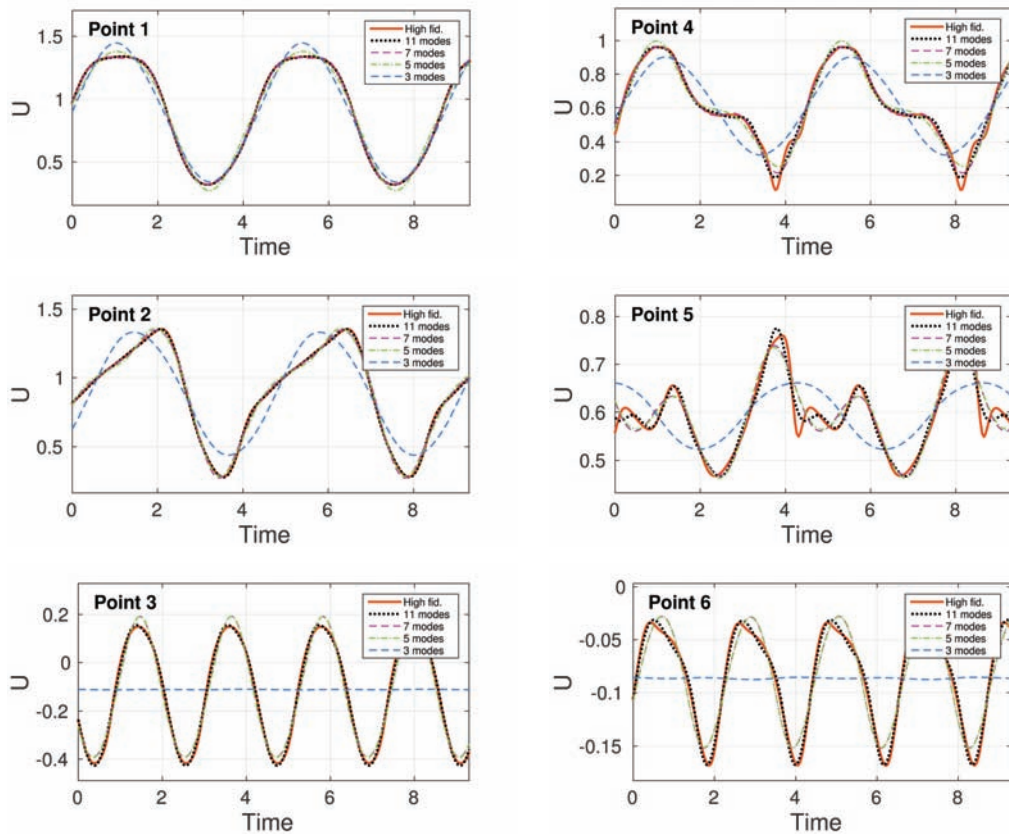


Figure 2.24: Time evolution of the streamwise high-fidelity and reconstructed velocity components for 3, 5, 7 and 11 modes.

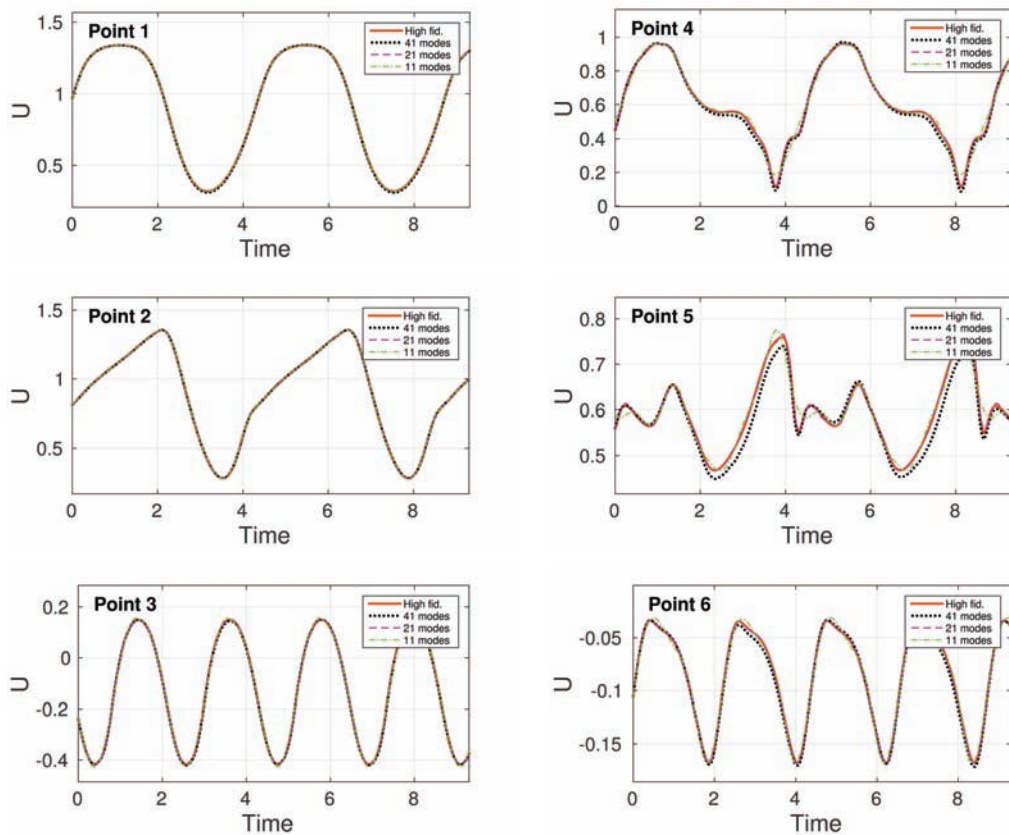


Figure 2.25: Time evolution of the streamwise high-fidelity and reconstructed velocity components for 11, 21 and 41 modes.

2.1.5 3D Simulations

Based on the results presented in the previous subsection, 3D simulations have been carried out by our research team. Some of them have been published ([Skopek et al., 2012](#)) and are briefly recalled here for comparison purpose. DDES- k - ω -SST and DDES- k - ω -OES simulation have been performed on a 3D mesh of 16 million volumes cells. The span of the domain was $H/D = 3$.

A slice of the 3D field is plotted in Fig. 2.26, and can be compared to the field of vorticity from 2D k - ω -SST simulation (Fig. 2.5). As expected, the resolution of the eddy structures is much better in the case the hybrid modelling, which compared well with the experiment in a qualitative point of view (Fig. 2.27). In particular the shear layer from the detachment point, at top and bottom of the two cylinders, is better defined, and the Kelvin-Helmholtz vortices are well captured.

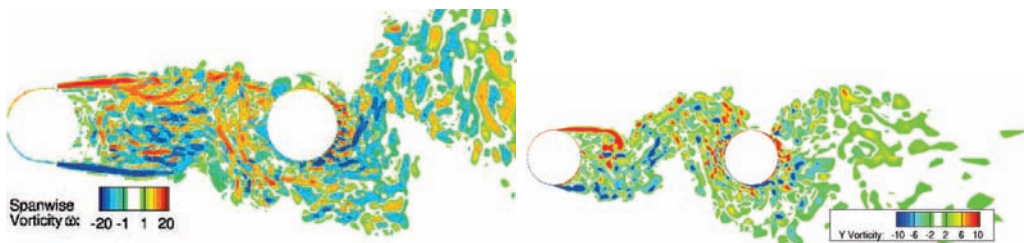


Figure 2.26: 2D view (slice) of the instantaneous spanwise vorticity field (left: DDES- k - ω -SST, right: DDES- k - ω -OES; [Skopek et al., 2012](#)).

Similarly to the 2D simulation (Fig. 2.7) mean streamlines have been plotted in Fig. 2.28 allowing for a direct comparison between experiment (PIV) and 3D simulation (DDES- k - ω -OES) in the gap region. At first glance, it seems the numerical result matches better the experimental one. The comparison of the mean streamwise velocity profiles in the gap region and downstream the rear cylinder (Fig. 2.29) confirms this observation.

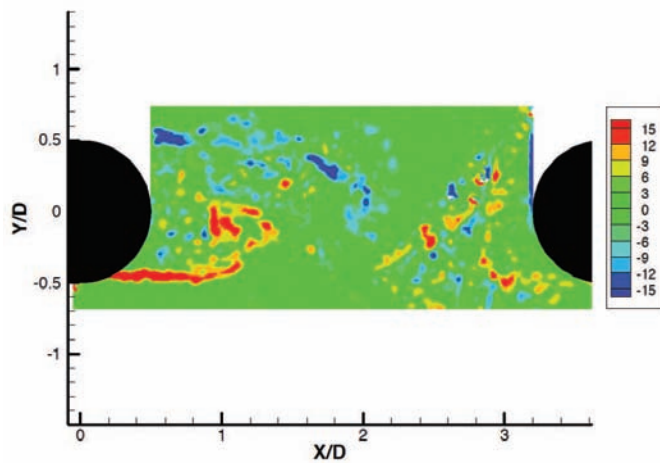


Figure 2.27: Instantaneous spanwise vorticity field from PIV measurements (Jenkins et al., 2005).

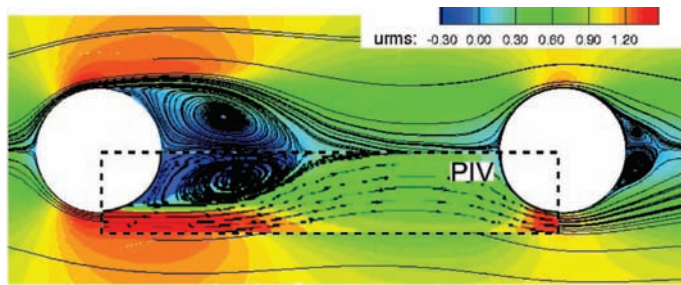


Figure 2.28: Mean velocity streamlines and field comparison between PIV and DDES- k - ω -OES (Skopek et al., 2012).

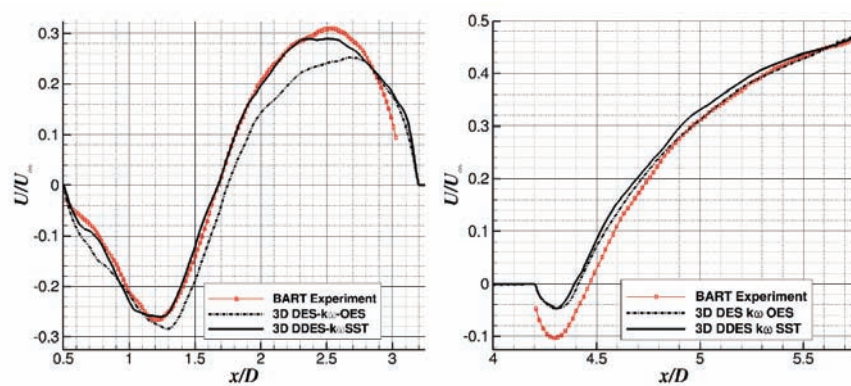


Figure 2.29: Mean streamwise velocity profiles comparison at $y = 0$ between PIV, DDES- k - ω -SST and DDES- k - ω -OES.

2.2 Fluid-structure interaction - Dynamic case

2.2.1 Introduction

The tandem cylinders configuration is related to the sizing of the heat exchangers in nuclear reactor technology. The configuration is also a model problem related to Movement Induced Vibration (MIV) dynamics extracted from a more complex cylinders bundle configuration as pointed out in the national research project ANR-Baresafe coordinated by EDF and including partnership of the main nuclear engineering industrial partners in France, CEA and AREVA. In this context, the objective is to propose High-Fidelity CFD-CSM approaches able to predict the loads (amplitudes and frequencies) as a function of the structural parameters (reduced velocity and the mass-damping number; Scruton number) with sufficient accuracy as required for design. Furthermore, the objective is to develop efficient low-order decomposition and reconstruction of the flow dynamics coupled with the structural dynamics, for further use in Reduced Order Modelling (ROM) which will enable faster design cycles for the end user. The present thesis aims at providing efficient turbulence modelling for the CFD part, coupled with the solid structure's motion by means of the Arbitrary Lagrangian-Eulerian method (ALE) and to simulate the spontaneous vibrational instability onset, when the structural parameters coupled with the fluid's velocity and time scales overpass critical limits.

Beyond the static configuration studied in the ATAAC European programme and as a link with the ANR-Baresafe program, the fluid-structure interaction will be examined, leading to vibration of the downstream cylinder in the tandem, because of the shearing mechanisms and vortex shedding developed past the upstream cylinder. This problem is also related to the vibrations occurring in the landing gear cylindrical supports.

A suitable POD reconstruction will be presented applied to the vibrational case, on view of further use in the Reduced Order Modelling context.

2.2.2 Results

2.2.2.1 Fluid-structure interaction

Fig. 2.30 presents the evolutions of the lift coefficient in comparison with the position of the downstream cylinder versus time, for Scruton number $Sc = 1$. For low values of the reduced velocity up to 3, these evolutions are in phase, showing synchronisation between the force and displacement. This indicates a 'lock-in' mechanism corresponding to the Vortex Induced Vibration (VIV) as depicted also in the simulations by Shinde et al. (2014) in a cylinders bundle configuration. At reduced velocity value of 4, a slight phase lag occurs, which becomes more pronounced and progressively increases in the reduced velocity range [5, 10]. This behaviour indicates the passage to the Movement Induced Vibration (MIV), where the phase lag increases and is associated to vibrational instability which can lead to negative damping (Fig. 2.31).

The Strouhal number of the lift oscillations does not considerably vary as a function of the reduced velocity (Table 2.6). The Strouhal number of the downstream cylinder position is practically constant in the VIV range and decreases in the MIV

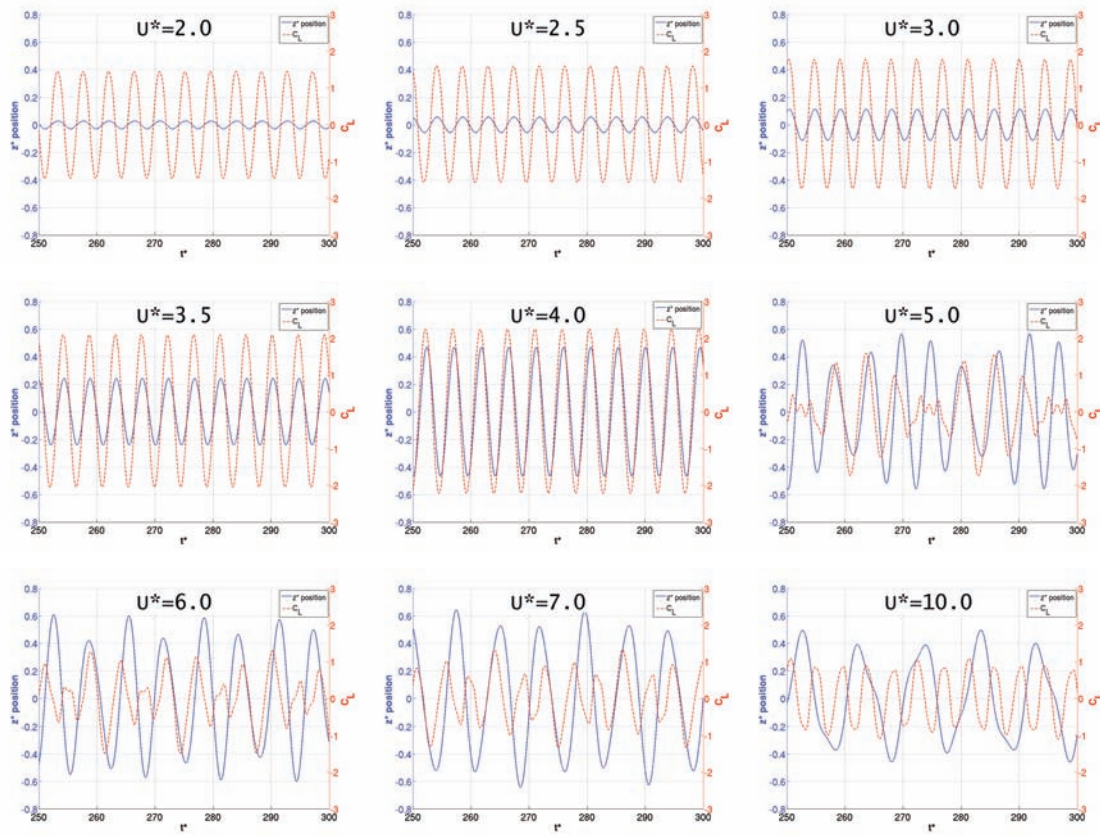


Figure 2.30: Position and lift coefficient of the downstream cylinder for reduced velocities between 2.0 and 10.0.

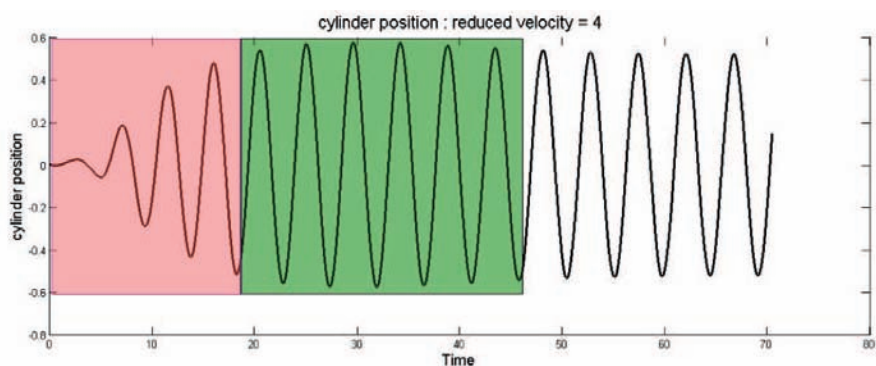


Figure 2.31: Transitional phase of the cylinder vibrations (red: amplification, green: saturation).

\mathbf{u}^*	2.0	2.5	3.0	3.5	4.0	5.0	6.0	7.0	10.0
St(\mathbf{C}_L) Up.	0.228	0.227	0.227	0.222	0.212	0.227	0.228	0.227	0.228
St(\mathbf{C}_L) Down	0.228	0.227	0.227	0.222	0.212	0.181	0.228	0.227	0.228
St(\mathbf{z}^*) Down	0.228	0.227	0.227	0.222	0.212	0.181	0.155	0.135	0.098

Table 2.6: Comparison of Strouhal numbers vs reduced velocities in dynamic case (Up.: upstream cylinder, Down: downstream cylinder).

range of the reduced velocities. This behaviour is also shown in Fig. 2.32, where the values are reported. In this figure, f_{S0} corresponds to the non-dimensionalised natural frequency of the cylindrical structure.

Fig. 2.35 shows the flow structure from the Q -criterion for the DDES- k - ω -OES computations of the vibrational case with Scruton number of 1 and reduced velocity of 3. The spanwise vortex structures past the downstream cylinder undergo a drastic modification of their wavelength, which displays strong dislocation patterns regarding the static case (Skopek et al., 2012). A 3D-POD analysis is under progress in order to provide a space-time tracking as presented in Szubert et al. (2015b) and discussed in section 3.1.1 page 52 for the flow around a supercritical aerofoil. A two-dimensional view of the flow pattern is provided in Fig. 2.33 and 2.34 in the section dedicated to the POD analysis.

2.2.2.2 POD analysis

Similarly to the static case (subsection 2.1.4.4 page 27), an attempt of POD analysis is carried out in the dynamic case.

Fig. 2.33 and 2.34 show the result after POD analysis carried out for the dynamic case. Because of the moving boundary of the downstream cylinder, POD has been applied on the number of snapshots classified according to a phase-splitting of the displacement evolution within 8 intervals within one period of von Kármán vortex shedding. In each interval, the hypothesis of small displacement has been made. Snapshots were recorded at the simulation time step, $\Delta t^* = 0.00845$. The POD reconstructions are compared with instantaneous fields of different phases at $0 \times T_{VK}$ and $T_{VK}/4$ in the first figure, and $2T_{VK}/4$ and $3T_{VK}/4$ in the second figure, where T_{VK} is the period of the von Kármán vortex shedding. A good comparison has been obtained regarding the moving grid in the context of the fluid-structure interaction.

This kind of POD reconstruction is promising to use for the construction of a Reduced Order Model, where the present POD basis can be used for the Galerkin projection of the present High-system of transport equations. This issue is being used in the context of the ANR-Baresafe research project.

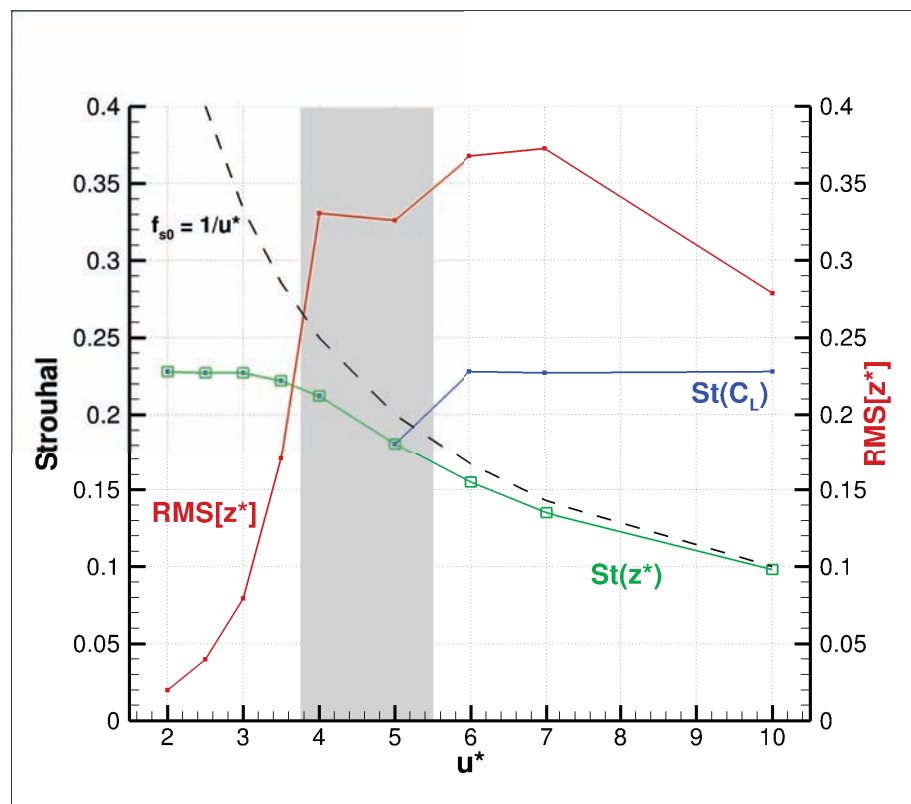


Figure 2.32: Non-dimensionalised frequency of the lift coefficient (blue) and position of the downstream cylinder (green) and RMS value of the position fluctuations (red).

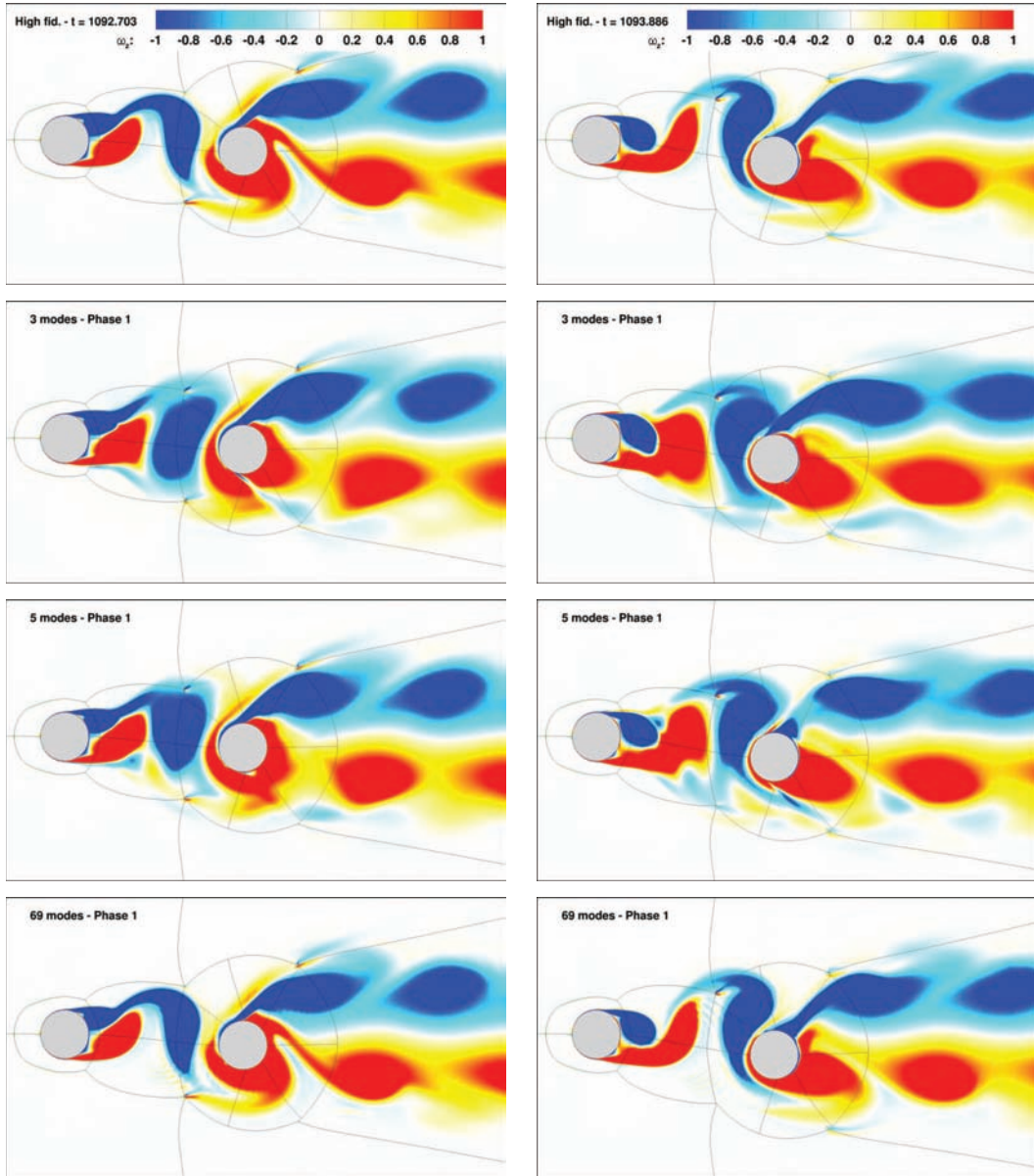


Figure 2.33: Vorticity field from URANS (top) and POD reconstruction from 3, 5 and 69 modes at $0 \times T_{VK}$ (left) and $T_{VK}/4$ (right) in dynamic case.

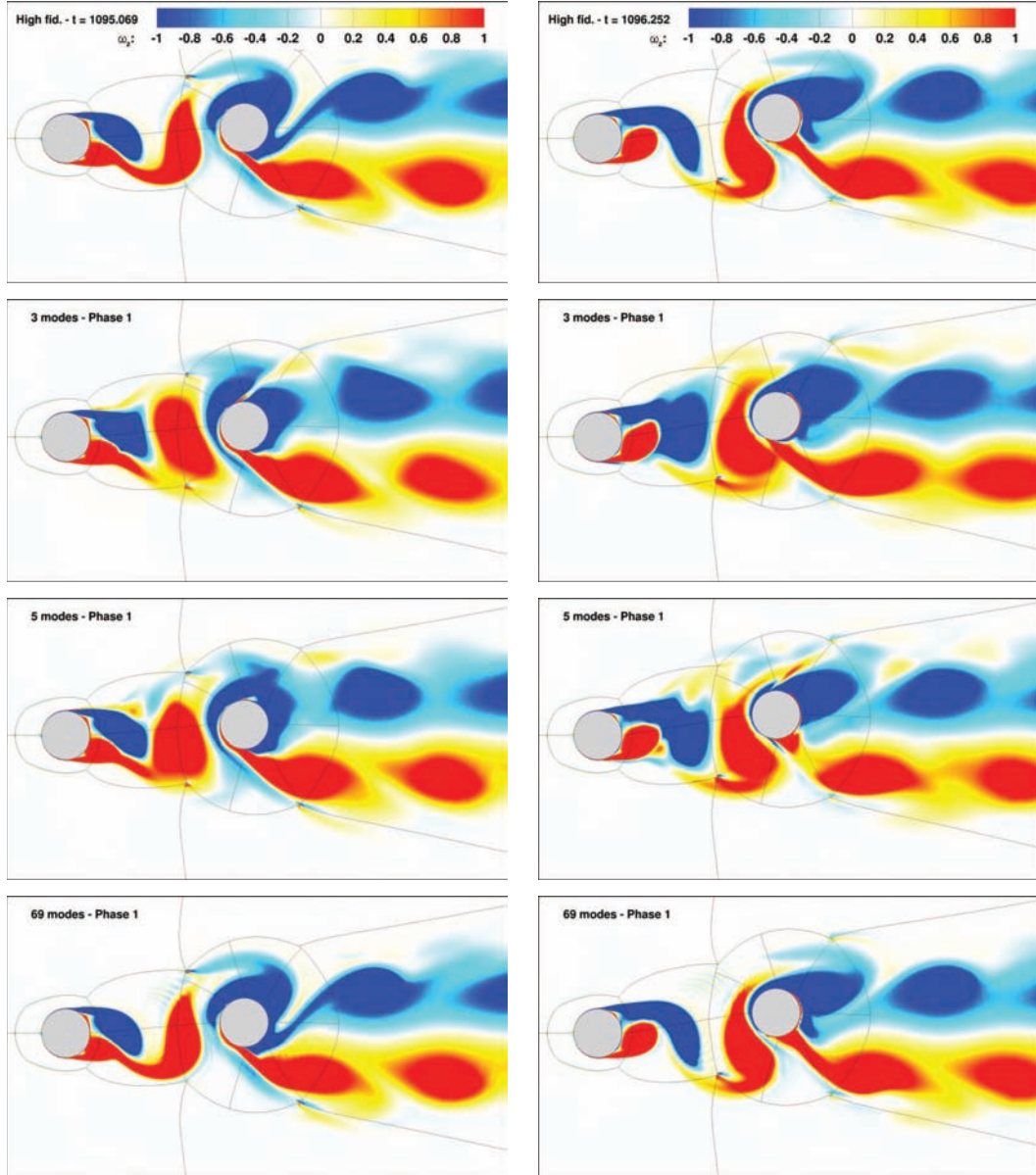


Figure 2.34: Vorticity field from URANS (top) and POD reconstruction from 3, 5 and 69 modes at $2T_{VK}/4$ (left) and $3T_{VK}/4$ (right) in dynamic case.

2.3 Conclusion

2D simulations of the tandem cylinders configuration have been performed to determine the optimal convergence criterion, as well as to study the capability of three turbulence models to predict the flow around this geometry, compared to experimental results. All these results have been used for DDES computations ([Skopek et al., 2012](#)), that highlighted the importance of the third dimension in the prediction , and confirmed that classical URANS modelling is not suitable to capture high-frequency phenomena, in particular in the noise range. However, hybrid modelling was able to predict with high accuracy these phenomena, as well as the mean flow properties.

The present study has shown the ability of spontaneous oscillatory motion generation on the downstream cylinder, which was allowed moving freely in the vertical direction along the lift coefficient. The computations have shown the passage from the VIV lock-in mechanism towards the MIV mechanism of vibrational instability characterized by negative damping. The corresponding progressive increase of the phase-lag from zero (in the VIV case) to higher values (in the MIV case) reaching also phase opposition by 180° has been quantified, as well as the appearance of negative damping in the transient phases of the motion. This behaviour is in qualitative agreement with the Connors experimental diagram as well as with other DDES simulations in the context of the ANR-Baresafe program ([Shinde et al., 2014](#)). These simulations predicted the von Kármán instability frequencies as well as the evolution as a function of the reduced velocity, of the von Kármán mode Strouhal number and of the RMS of lift coefficient. The fluid-structure interaction is currently being studied by means of hybrid DDES simulations aforementioned Fig.[2.35](#))

Based on the present High-Fidelity approaches, the present thesis carried out a POD reconstruction of the static and dynamic structural oscillation flow cases, by using an adapted phasing of the POD snapshots in the dynamic case. The provided reconstructions are able to capture the principal dynamics of the flow field and the method is currently in use in the Baresafe context for the Reduced Order Modelling of the dynamic case.

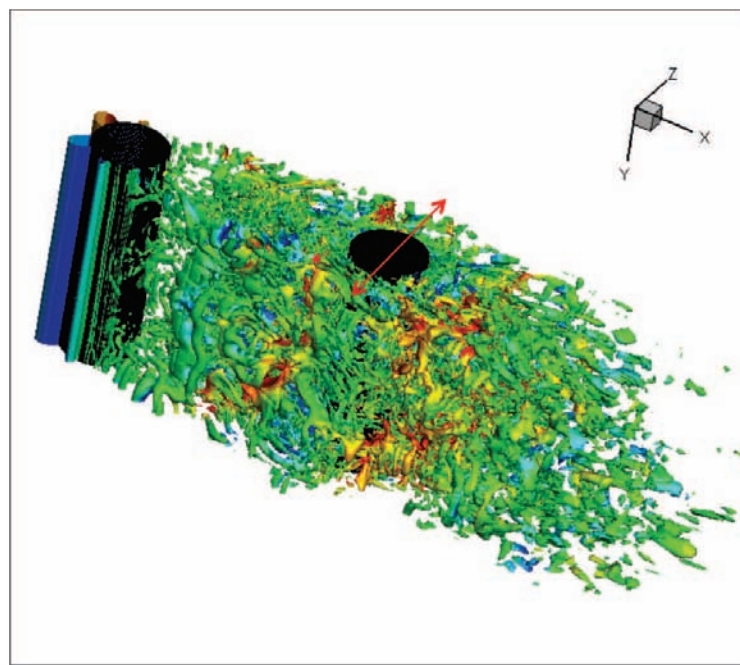


Figure 2.35: Q criterion field around the tandem cylinders in 3D and dynamic configuration by DDES-OES- k - ω -BSL.

Lire
la seconde partie
de la thèse